Interplay between tectonics and surface processes in the evolution of mountain ranges: Insights from landscape dynamics, uplift, and active deformation of Talesh Mountains (NW Iranian Plateau margin)

Mohammad Moumeni [a,*], Michele Delchiaro [a], Marta Della Seta [a], Reza Nozaem [b], Paolo Ballato [c], Joel S. Leonard [d], Romano Clementucci [c,e], Javad Rouhi [a]

[a] *Department of Earth Sciences, Sapienza University of Rome, Rome, Italy*
[b] *School of Geology, College of Science, University of Tehran, Tehran, Iran*
[c] *Department of Sciences, Roma Tre University, Rome, Italy*
[d] *Department of Geosciences, Colorado State University, Fort Collins, CO, USA*
[e] *Department of Earth Sciences, ETH Zürich, Zürich, Switzerland*

ARTICLE INFO

ABSTRACT

Drainage divides are dynamic features of a landscape that migrate over time during the development of river networks. In this study, we focused on the geomorphic response of a landscape to the interaction among tectonics, climate, and lithology in the Talesh Mts. along the northwest of the Iranian Plateau. The footprints of these competing forces have been analyzed by divide stability analysis and applying χ, χ_Q, and Gilbert metrics. Additionally, we examined the effects of bedrock erodibility on landscape evolution processes by measuring the mechanical rock strength of the lithological units in different sectors of the mountain range. The distribution of the χ values suggests a disequilibrium of the drainage networks across the whole main divide and its tendency to migrate towards the interior of the plateau. In contrast, Gilbert metrics, which focuses on a narrow topographic zone across the divide, suggest that the uppermost divide in the northern and southern Talesh Mts. is stable. Moreover, asymmetry in Gilbert metrics across the central part of the range suggests that the divide might be migrating towards the plateau interior. The possible scenario for the whole divide's behavior is associated with the contrasting erosion rates across the divide. In the northern and southern sectors of the Talesh Mts. range, the erosional wave related to the most recent uplift pulses has not reached the divide yet. Mechanism of topographic rejuvenation is controlled by heterogeneous uplift of strong bedrock units in the northern and southern sectors, and weak bedrock units outcropping in the central sector, initiated topographic rejuvenation largely in the central Talesh Mts. Parallelly, the precipitation has a limited effect in assisting and magnifying the divide mobility, reorganization, and landscape transience. In general, we can infer that divide is in a transient state due to the spatially varying rock uplift and bedrock erodibility.

1. Introduction

The interaction between climate, tectonics, and lithology often occurs in mountainous environments, making it challenging to separate and measure their individual influences on shaping the topography and erosion processes. In dynamic mountain-building regions, surface processes encompass erosion and sediment deposition mechanisms, influenced by the intricate interactions between tectonic and climatic forces (e.g., Whipple et al., 2013; Lague, 2014; Adams et al., 2020; Delchiaro et al., 2022). In long timescales, tectonics has fundamental control on

base level and drainage divide movement in regional scales (e.g., Ye et al., 2022). Based on Leonard and Whipple (2021) if erosional processes in the landscapes which experience orographically enhanced precipitation are sensitive to spatial and/or temporal variations in precipitation, then changing orographic precipitation patterns should influence mountain landscape evolution. In addition to tectonics, and climatic variations, drainage divides migrate in response to difference in rock strength, stratigraphic and structural configuration of the lithological units, and erosion rates (Fig. 1) (Willett et al., 2014; Forte et al., 2016; Zondervan et al., 2020a; Clementucci et al., 2022). The rock

---
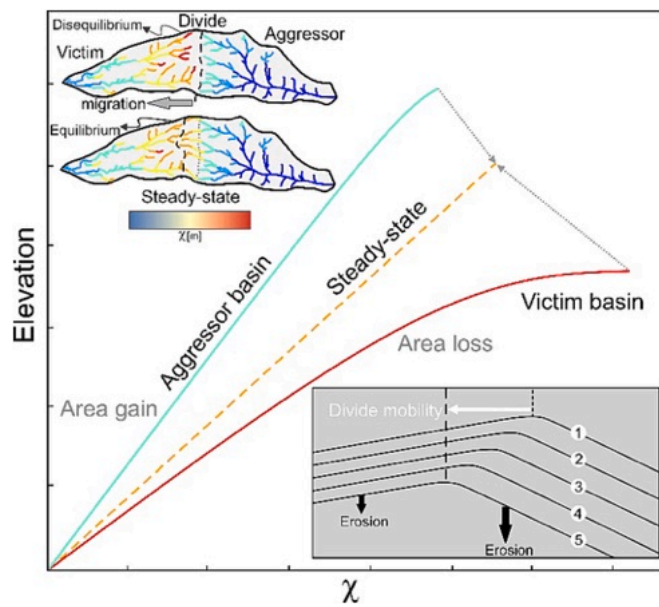
Fig. 1. Divide mobility, equilibrium and disequilibrium state of river basins and profiles (modified and readapted after Willett et al., 2014; Forte and Whipple, 2018). The inset (lower right) is a Schematic diagram of Gilbert's (1877) 'Law of Unequal Declivities'. Based on this law, due to unequal erosion rates across the divide, divides will move towards the side with lower erosion rate. This contrast in erosion rate is probably driven by differences in topographic gradient on both sides of the divide (e.g., Forte and Whipple, 2018).

strength exerts control on the landscape evolution of mountainous regions by (1) governing the ability of material to be removed, displaced, and transported by surface processes (e.g., Gilbert, 1877; Hack, 1957; Schmidt and Montgomery, 1995; Townsend, 2022), and (2) local relief expression by controlling the hillslopes (e.g., Whipple and Tucker, 1999). It is also suggested that rock fracture density rather than rock strength controls the river erosion process (e.g., Molnar et al., 2007). In a study by Zondervan et al. (2020a, 2020b), the drainage divide migration in the High Atlas in NW Africa attributed to the different lithologically and structurally groups of bedrock. They proposed that the rock erodibility variation alone can influence drainage divide mobility in a collisional mountain belt.

Thus, understanding the geomorphic response of a landscape, both along the river network and its drainage divide, is necessary to investigate the interactions among tectonics, climate, and lithology as they record crustal deformation and strain accumulation over long timescales (e.g., Willett, 1999; Whipple, 2009; Expósito et al., 2022; Delchiaro et al., 2023).

The Talesh Mts. are a prominent tectonic feature of the NW sector of the Iranian Plateau, which is formed by the compressional stresses transferred across the Arabia-Eurasia continental collision.

In previous studies in the Talesh Mts., Madanipour et al. (2013) documented three phases of exhumation by using detrital apatite fission track data in the Oligocene, early to middle Miocene, and early Pliocene. They suggest that the late Oligocene slow rock exhumation which accelerated in the middle Miocene resulted in the recent high-elevation and geometry of the range (Madanipour et al., 2017). The latter is suggested to be the onset time of deformation in the Talesh Mts. Madanipour et al. (2018) suggest that the orientation and timing of deformation was greatly impacted by the South Caspian block (SCB) and regional differences in the convergence direction related to the evolution of the Iranian Plateau. Moreover, it has been proposed that Caspian Sea base-level fall due to its isolation from the Paratethys domain, is responsible for the late Miocene-early Pliocene incision and rapid exhumation of the mountain range (Madanipour, 2023).

However, a comprehensive study of the effects of these tectonic uplift

and deformation phases, along with lithological characteristics and orographic rainfall on the landscape, and their impression on the geomorphological architecture of the study area is still lacking.

The present study focuses on the geomorphic response of the river network and drainage divides to the combined contributions of tectonic uplift, orographic precipitation, and lithological variations of the Talesh Mts. (Figs. 2 and 3). Investigating the interaction between these factors and isolating the role of each yields an applied procedure to reveal the main governing agent/s controlling the architecture of present-day landscape, and its evolutionary path. We combined a quantitative analysis of the main drainage divide with stream profiles in order to decipher the surface deformation, uplift mechanisms and drainage divide evolution. Moreover, we isolated the effects of rock strength contrasts on the landscape evolution processes by measuring the mechanical rock strength and calculating uniaxial compressive strength (UCS) of the lithological units in the three sectors of the mountain ranges. We also measured the channel metrics (i.e., k_{sn} and χ) by combining them with mean annual rainfall (k_{snQ} and χ_Q; Adams et al., 2020; Leonard et al., 2023) to isolate the climate effects.

Together, our results show the potential impact of the combined effects of orographic rainfall and variability of rock strength in the mobility of divide and landscape evolution of mountain ranges.

2. Regional framework

2.1. Geological setting

The Iranian Plateau is part of the Alpine–Himalayan system of mountain belts (Stocklin, 1968; Ghorbani, 2013) that extends from the Atlantic Ocean to the Western Pacific. The Plateau is a large actively deforming region that developed in response to the late Eocene to early Miocene collision between the Arabian and Eurasian plates (e.g., Allen et al., 2004; Ballato et al., 2011; Agard et al., 2011; Mouthereau et al., 2012; McQuarrie & van Hinsbergen, 2013 and references therein) (Fig. 2). Stress was subsequently transferred from the collision zone to the northern margin of the Iranian Plateau (e.g., Berberian, 1983; Jackson et al., 2002; Allen et al., 2003; Guest et al., 2006; Yassaghi and Madanipour, 2008; Ballato et al., 2008 and 2017; Madanipour et al., 2018). The spatial and temporal evolution of deformation at the northern sectors of the Arabia- Eurasia collision zone seems to result from the interplay between the rigid South Caspian Basin (SCB) in the north and the Central Iranian Block to the south (Fig. 2; e.g., Allen et al., 2003; Ballato et al., 2013). The Iranian Plateau represents an elongated, thickened, and low-topographic relief morphotectonic province and includes actively deforming orogenic belts (Vernant et al., 2004; Ballato et al., 2013, 2017). Surface processes may have significantly contributed to redistributing mass, thereby influencing the shallow crustal stress field and fault activity (Ballato et al., 2015). GPS vectors indicate that the general direction of crustal motion in NW of Iran, respect to a fixed Eurasian frame, is towards the north at rates of 22–23 mm/yr (Fig. 2) (Vernant et al., 2004; Reilinger et al., 2006). The Talesh Mts. at the NW border of the Iranian Plateau are part of the Arabia-Eurasia collision zone (Fig. 3) and connect the Alborz Mountains with the Lesser Caucasus. The orogen has a curved geometry that bends around the southwestern margin of the SCB from EW to NW and WNW (e.g., Berberian, 1983; Jackson et al., 2002; Allen et al., 2003; Madanipour et al., 2013, 2017). The onset of mountain building and exhumation in the Talesh Mts. is Eocene-Oligocene (Madanipour et al., 2018) and is interpreted as the initial stage of the Arabia-Eurasia continental collision (e.g., Allen et al., 2004; Ballato et al., 2011, 2013; Madanipour et al., 2017, 2018). Since the Miocene, these mountains form an orographic and topographic barrier that separates the Ardebil Basin (interior of the plateau) from the coastal plains of the Caspian Sea (Fig. 3). GPS data show clockwise rotation of the SCB with respect to the Talesh Mts. (Djamour et al., 2010, 2011). Additionally, complex deformation at the northwestern Iranian Plateau is reflected in seismicity at the western edge of the SCB and the
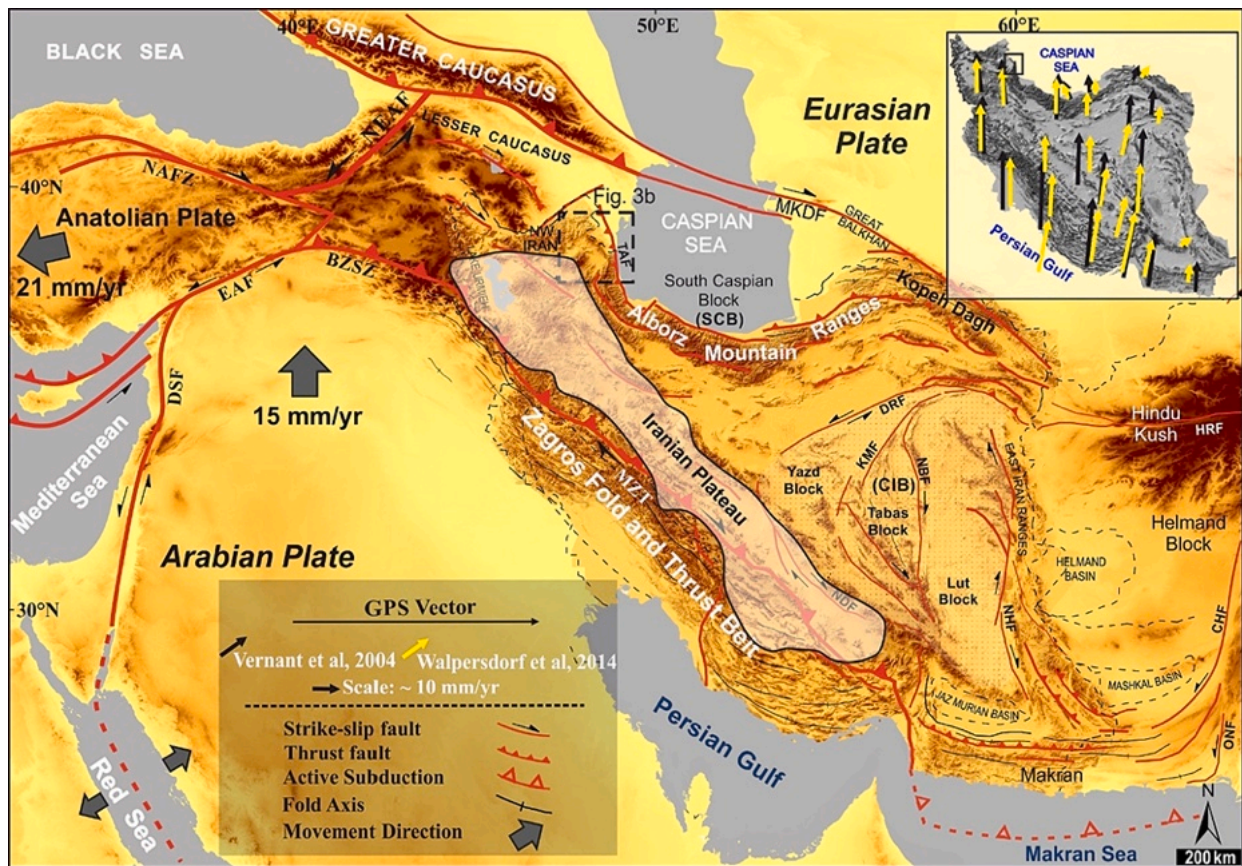
Fig. 2. Simplified tectonic map of the Arabia- Eurasia collision zone. Shaded-relief of Shuttle Radar Topography Mission (SRTM) (Farr et al., 2007) digital elevation model, showing the main tectonic domains, blocks and the major fault systems accommodating the Arabia-Eurasia convergence. White highlighted area shows the Iranian Plateau boundary. Abbreviation is: MKDF: Main Kopet Dagh Fault, MZT: Main Zagros Thrust, DRF: Doruneh Fault, TAF: Talesh Fault, HRF: Herat Fault, NHF: Nehbandan Fault, CHF: Chaman Fault system, ONF: Ornach-Nal Fault, KMF: Kalmard Fault, NDF: Nain-Dehshir Fault, NBF: Nayband Fault, BZSZ: Bitlis Zagros Suture Zone, EAF: East Anatolian Fault, NAFZ: North Anatolian Fault Zone, NEAF: North-Eastern Anatolian Fault, DSF: Dead Sea Fault. The inset (upper right), shaded relief map shows GPS vectors in Iran relative to stable Eurasia; the data is obtained after Vernant et al., 2004 (black arrows), and Walpersdorf et al., 2014 (yellow arrows); Location of the study area in the NW of Iran is indicated by black dashed square.

Talesh Mts. (e.g., Jackson et al., 2002; Madanipour et al., 2018). A minor component of underthrusting of the SCB lithosphere beneath the continental crust of the Talesh Mts. is suggested by seismic and gravity data (e.g., Berberian, 1983; Jackson et al., 2002; Allen et al., 2003).

The Talesh Mts. are composed of Paleozoic to Quaternary rock units. Paleozoic strata include volcanic, clastic, and carbonate rocks (Fig. 3a). Mesozoic rock units consist primarily of Triassic to Lower Jurassic carbonates and clastics. Cenozoic strata (~8 km of thickness) are chiefly composed of volcanic and volcaniclastic rock units (Fig. 3a) that are mostly associated with Eocene magmatism in rapidly subsiding marine basins (Berberian and King, 1981; Vincent et al., 2005; Madanipour et al., 2013, 2018). In the northern and central sectors of the Talesh Mts., Cenozoic sedimentary, volcanic, and volcaniclastic sequences are widely exposed, while older rock units crop out solely in the core of some anticlines (e.g., Madanipour et al., 2013, 2018; and references therein; Fig. 3a).

2.2. Morphological and climatic setting

The geometry of the range highlights the extent of the elevated axial surface with local variations in topographic relief, mountain peaks and incised valleys. The high-standing landscape in the northern and southern sectors are mainly composed of Eocene andesite and volcaniclastic rocks.

In the eastern part of the main drainage divide in the wet flank of the range, the topography is dominated by several large anticlines and thrust faults (Fig. 3). This topographic contrast between the two sides of the divide is also reflected in the spatial variations of the topographic gradient, distribution of relief, elevation, and precipitation. The occurrence of orographic barriers intercepting moisture sourced in the Caspian Sea determines the disparate distribution of precipitation (e.g., Zaitchik et al., 2007; Ballato et al., 2010 and references therein). In the late Cenozoic, Iran experienced significant long-term and short-term climatic variations, which most likely influenced erosional and depositional processes (Ballato and Strecker, 2014). Central and northern Iran was characterized by a hot, arid climate since the late Eocene (Jackson et al., 1990; Davoudzadeh et al., 1997). On the other hand, moisture from the Caspian Sea could have been forced into concentrated precipitation along the uplifting Alborz ranges (Ballato, 2009 and references therein). During the early-middle Miocene the Alborz range became an efficient orographic barrier as suggested by paleoclimate data (Ballato et al., 2010). The N-NW-trending Talesh fault which bounds the central and northern sectors of the Talesh Mts., with Masuleh Dagh (MD), and Boghrov Dagh (BD) faults on the southern flank of the range are the main active structure, which promotes the recent growth of relief and topographic barrier to the moisture sourced from Caspian Sea. The orographic barrier controls the spatial variability of climate by enhancing precipitation towards the Caspian Sea and aridity in the interior of the plateau.

The positive feedback between orographically induced precipitation and rock-uplift rates must have been established only recently along the northern slope of the Alborz (e.g., Ballato et al., 2015). At present,
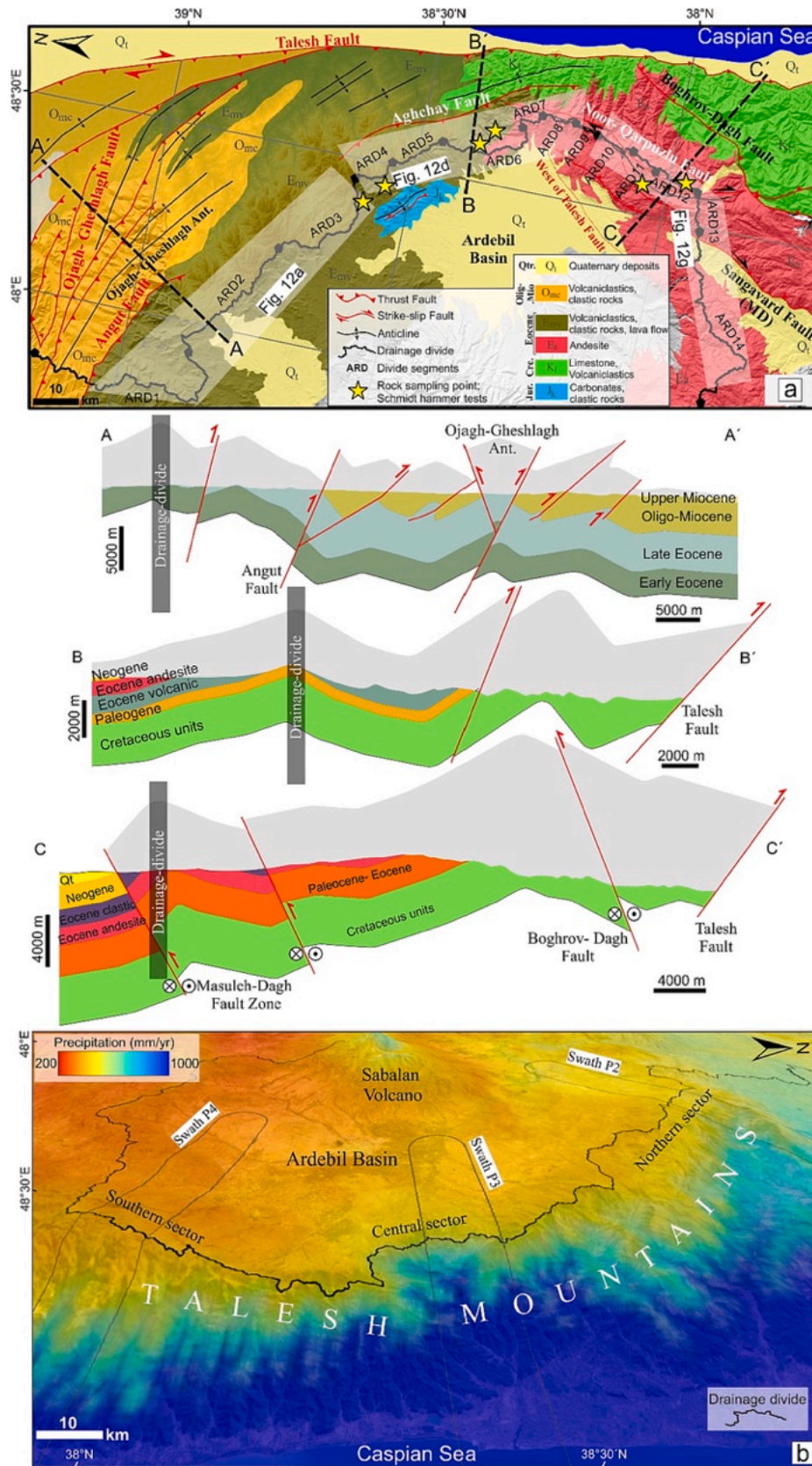
(caption on next page)

Fig. 3. (a) Geological map and cross sections of the study area with main structures and lithological units, modified and readapted after Madanipour et al. (2017, 2018); Vincent et al. (2005), Geological Survey of Iran (1975, 1999). The grey-shaded areas above the topography are the exhumed part of the section constructed based on the geometry and kinematics of the main structures. Location of the Ardebil Basin's main drainage divide in Talesh Mountains represented on the structural cross-sections (grey vertical stripes) and geological map. The main divide has been divided into fourteen segments (ARD1-ARD14) to calculate the Gilbert metrics and χ (see methods). The white polygons indicate the north, central, and southern parts of the divide in Talesh Mountains. (b) Digital elevation model with superposed average 30-years annual precipitation pattern from 1970 to 2000 of the NW of Iran. The data with 30 s (~1 km²) spatial resolution is acquired from WorldClim version 2.1 (Fick and Hijmans, 2017) climate database. P2 to P4 show the locations of the 20-km-wide swath profiles of rainfall which are shown in Fig. 15b-d.

roughly 1000 mm/yr of precipitation falls along the coast of the Caspian Sea on the northern flank of the Talesh Mts. in the western Alborz ranges (Fig. 3b). In contrast, the Ardebil Basin and the plateau interior regions receive <300 mm/yr of rainfall that is mostly sourced from the westerly winds.

2.3. Fluvial topographic metrics

In unglaciated settings, bedrock river longitudinal profiles record information about tectonics, climate, and erodibility of the bedrock lithology (e.g., Kirby and Whipple, 2012). Observations from these rivers show that the local channel slope (S) can be described as a power-law function of the upstream drainage area (A):

$$S = k_s A^{-\theta}, \tag{1}$$

where k_s is the channel steepness index and θ is the concavity index (e.g., Flint, 1974; Whipple et al., 2022). Alone these indices have limited use for regional geomorphic investigation because k_s and θ are strongly correlated, which precludes direct comparisons between different rivers. Based on the observation that natural river profiles that appear to be in morphological equilibrium (i.e., graded profiles) exhibit a narrow range of concavity index (e.g., Wobus et al., 2006), the concavity index is often fixed to a reference value (θ_{ref}) to obtain the normalized channel steepness index (k_{sn}), which allows quantitative comparisons of steepness between rivers of different size:

$$k_{sn} = S A^{\theta_{ref}}. \tag{2}$$

The normalized channel steepness, k_{sn}, has been shown to correlate with erosion rates in diverse settings but it is expected that climate and bedrock lithology, among other factors also affect k_{sn} (e.g., Kirby and Whipple, 2012; Lague, 2014; Whipple et al., 2022). Determining the degree to which climate impacts topography continues to be a significant challenge (Montgomery et al., 2001; Burbank et al., 2003). Since the k_{sn} is reliant on upstream drainage area as a discharge proxy it assumes that climate is uniform, which has been shown to be a limitation for identifying the effect of climate (e.g., Adams et al., 2020; Leonard and Whipple, 2021; Leonard et al., 2023). Weighting mean-annual rainfall (MAP) into channel steepness has been shown to be an effective way of capturing the effect of climate (Adams et al., 2020; Leonard et al., 2023), resulting in the normalized channel steepness variant k_{snQ}:

$$k_{snQ} = S Q^{\theta_{ref}}. \tag{3a}$$

$$Q = PA, \tag{3b}$$

where Q is an improved discharge proxy and P is the upstream average rainfall. Notably, k_{snQ} is analogous to unit stream power and similar metrics (e.g., Finlayson et al., 2002; Bookhagen and Strecker, 2012), and should better reflect erosion rates where rainfall is spatially variable.

A practical way to visualize channel steepness patterns and thus potentially spatial variations in erosion rate and divide migration is by using the χ-transform (e.g., Perron and Royden, 2013; Willett et al., 2014). This transformation scales the horizontal coordinate (x) to account for the expected covariation between slope and drainage area with distance along the river longitudinal profile, such that:

$$z(x) = z(x_b) + \left(\frac{k_{sn}}{A_0^{\theta_{ref}}}\right)\chi \, dx, \tag{4a}$$

$$\chi = \int_{x_b}^{x} \left(\frac{A_0}{A(x)}\right)^{\theta_{ref}} dx, \tag{4b}$$

where z is elevation, x_b is the baselevel position, and A_0 is an arbitrary reference area set to 1 km². Provided θ_{ref} is set appropriately, a river profile with uniform k_{sn} will be linear in χ-z plots, whereas profiles with variable k_{sn} show changes in slope χ-z plots (e.g., due to spatial or temporal variations in uplift rate, rainfall, lithology). Similar to k_{sn} and k_{snQ}, the effect of rainfall on channel steepness can be weighted into χ to yield χ_Q (e.g., Perron and Royden, 2013; Yang et al., 2015; Leonard et al., 2023):

$$z(x) = z(x_b) + \left(\frac{k_{snQ}}{A_0^{\theta_{ref}}}\right)\chi_Q \, dx, \tag{5a}$$

$$\chi_Q = \int_{x_b}^{x} \left(\frac{A_0}{Q(x)}\right)^{\theta_{ref}} dx. \tag{5b}$$

Importantly, the above metrics are measured from the fluvial topography of the landscape and do not require the Stream Power Incision Model (SPIM) either for their derivation or for assessment of divide stability. To the extent that channel steepness values reflect erosion rates, these metrics can potentially identify erosional disequilibrium across drainage divides and thus divide migration (e.g., Fig. 1). However, this highlights an important limitation of using χ-based metrics to evaluate divide stability: spatial variations in erodibility that affect channel steepness mimic variations in erosion rate, which can potentially bias divide stability assessments. We can evaluate the effect of rainfall on erodibility using χ_Q but the effect of other factors like lithology must still be considered separately (Section 3.2) (Buscher et al., 2017; Forte and Whipple, 2018; Expósito et al., 2022). Integrating upstream from baselevel also means that spatial variations in erosion rate affect upstream values. Consequently, χ values may not necessarily reflect local erosional conditions at the drainage divide, and thus contrasts do not necessarily reflect current migration (e.g., Forte and Whipple, 2018).

Gilbert metrics (mean gradient, mean local relief, mean channel bed elevation) (Whipple et al., 2017; Forte and Whipple, 2018), originally postulated based on Gilbert's (1877) law of unequal slopes (Fig. 1), provide an alternative approach to assess divide stability, and focus on topography near the drainage divide where conditions are more likely to be uniform (Whipple et al., 2017; Forte and Whipple, 2018). Like χ and χ_Q, divide stability is interpreted from equal values in Gilbert metrics across the drainage divide, while unequal values may suggest ongoing or future divide motion. The use of the χ-based metrics in concert with the Gilbert metrics can give us more information for interpreting the potential condition of a divide, as disagreements among these different metrics may indicate ongoing adjustment non-uniform uplift rate and/or spatially/temporally variable erosional efficiency (Forte and Whipple, 2018).

3. Methods

3.1. Topographic analysis

To compute geomorphic indices, we used a 30-m digital elevation model (DEM) obtained by the Shuttle Radar Topography Mission (SRTM) (Farr et al., 2007), and a precipitation grid from WorldClim climate database (Fick and Hijmans, 2017). Stream networks and drainage divides were extracted and analyzed in MATLAB using software packages TopoToolbox (Schwanghart and Scherler, 2014), DivideTools (Forte and Whipple, 2018), and the Topographic Analysis Kit (Forte and Whipple, 2019). We extracted the stream network with a threshold area of 1 km^2 (Fig. S1) to define the channel head. We computed the reference concavity index (θ_{ref}) using the *mnoptim* function in TopoToolbox and use a value of $\theta_{ref} = 0.52$ for all analyses (Fig. S2). We analyzed the drainage network characteristics and divide stability by extracting knickpoints and channel metrics k_{sn} and χ, along with rainfall-weighted versions k_{snQ} and χ_Q, as well as Gilbert metrics (e. g., Perron and Royden, 2013; Forte and Whipple, 2018; Adams et al., 2020; Whipple et al., 2022; Leonard et al., 2023).

Furthermore, rivers in transient state with non-lithological knickpoints which mark an upstream relict landscape have been used to estimate the total magnitude of fluvial incision. We used the highest non-lithological knickpoints and calculated the difference between the reconstructed and modern longitudinal river profiles for this estimation.

Additionally, we created several swath profiles across and orthogonal to the main drainage divide to explore topographic characteristics, including local relief profiles and hypsometric integral (Hi Index; e.g., Pike and Wilson, 1971). To improve the description and the comparison of hypsometry along a swath profile, we rescaled Hi values and used the enhanced transverse hypsometric integral (Thi*) (Pérez-Peña et al., 2017), in which Hi values are weighted by the relative local relief. We combined topographic analysis with measurements of compressive rock strength through the utilization of a Schmidt hammer and point load test to supplement topographic analyses, described further in Section 3.2 below. The devised workflow of this study is represented in Fig. 4.

3.2. Rock strength mechanical measurements

The aim of this analysis is to estimate the degree of erodibility variation across different rock types, a key unknown that the topographic metrics described above are not able to account for directly. To achieve this, we applied a multi scale testing approach by using two indirect methods including Schmidt hammer rebound values and point-load test measurements and converting them to UCS. Additionally, we used geological strength index (GSI) of jointed rock mass (Hoek and Brown, 1997; Hoek et al., 2013) which is a qualitative index and enables us to estimate the strength of a rock mass based on visual inspection of rock outcrops in the fieldwork (Fig. S6). Thus, we can have a comparison of rock strength in the scale of rock matrix, rock mass and the entire outcrop. We conducted mechanical measurements of rock strength in the field using the Schmidt hammer rebound (e.g., Murphy et al., 2018; Zondervan et al., 2020a; Zondervan et al., 2020b; Chilton and Spotila, 2022), and took rock samples from the drainage divide to analyze in the laboratory by point load test (ASTM, 2008). We did the laboratory measurements and studies in the Laboratory of Engineering Geology, at the Department of Earth Sciences, Sapienza University of Rome.

3.2.1. Schmidt hammer rebound index

We used the Schmidt hammer Type-N which is utilized for supplying information on the types of rocks, weakness, and their compressive strengths. Schmidt hammer rebound measurements were collected across the entire divide in the north, central, and southern sectors of the mountain. A total of over 600 Schmidt hammer values were taken, with approximately 200 rebound readings recorded in each sector. In each sector, two representative samples were collected for specific gravity determination and natural gamma measurements with hydrostatic balance.

The reliability of results obtained using the Schmidt hammer index is often compromised by various factors such as the type of hammer, its orientation, the normalization of rebound values, specimen dimensions, weathering, etc. To address these issues, we used Schmidt hammer chart (Goudie, 2006). The estimation of uniaxial compressive strength (UCS) of the rock types in each sector of the mountain range has been determined by utilizing the average weight per unit volume obtained from laboratory tests (Tables S1-S3), the orientation of the hammer, the values of rock strength measured by Schmidt hammer, and plotting them on the Schmidt hammer chart.

3.2.2. Point load strength index (PLI)

We conducted point load tests to samples to supplement UCS results obtained from Schmidt hammer measurements, and to rule out the effects of rock discontinuities (Broch and Franklin, 1972; ASTM, 2008; Chilton, 2021). In accordance with the guidelines established by ASTM and ISRM (Franklin, 1985; ASTM, 2008), the point load tests on the samples were performed in the laboratory. We performed tests on samples from two sites in the north, two sites in central, and three sites in the south of the study area. We performed 15–20 tests on each sample resulting in a total of approximately 100 tests. The Point Load Strength Index was determined by applying a size correction based on the pre-test sample dimensions by following ISRM guidelines (Franklin, 1985). The data obtained from the tests was then converted to UCS using empirical
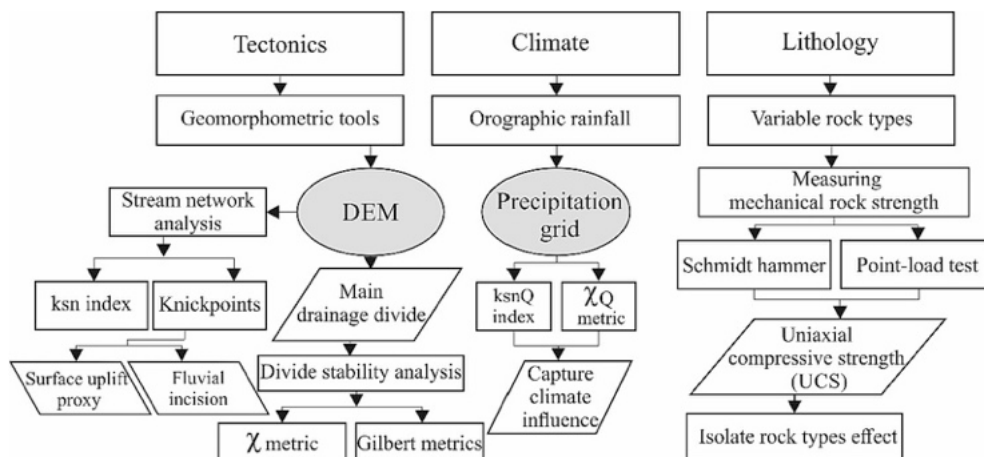

Fig. 4. Flowchart, and general workflow for isolating the contributions of tectonics, climate and lithology on present day topography.

equations (Tables S4-S6).

4. Results

4.1. Drainage divide stability evaluation

The general orientation of the drainage divide, as well as the strike and axial planes of the faults and folds, conforms to the strike of the mountain range (Fig. 3). Since a single divide may be heterogeneous, it is useful to segment a divide and assess the stability of these segments separately (Forte and Whipple, 2018). We segmented the Ardebil Basin main divide into 14 sections (ARD1 to ARD14) (Fig. 3a) to calculate the Gilbert metrics (Fig. S3b-d) and χ metric (Fig. S3a) and assess divide stability (Figs. 5–7). We segregated the main divide based on visual examination of all the metrics and chose the break points based on the catchments boundaries, between portions of the divide that show transitions in at least one of these criteria (Forte and Whipple, 2018).

The main drainage divide in the study area shows large across-divide contrasts of χ values (i.e., χ anomalies), which suggests the divide may be unstable (Figs. 5a; S3a). Locally, χ anomalies consistently indicate potential divide migration towards the interior of the plateau. Using the rainfall-weighted variant, χ_Q, these contrasts are enhanced, with χ_Q values that are two times higher than χ values (Fig. 5b). These more pronounced contrasts show the potential influence of spatially varying rainfall on the river profiles, and, accordingly, driving greater across-divide differences in erosion rates and divide motion.

In contrast, Gilbert metrics suggest the north and southern parts of the divide are largely stable (Figs. 6, and 7), with the exception of two segments (ARD11 and ARD12) in the southern part of the divide. In general, the southern part of the divide which is oriented NE-SW, located along the main structures where the local relief (Fig. S3d) and k_{sn} values are very high. Gilbert metrics suggest the divide segments in the central Talesh Mts. (ARD4 to ARD8) may be migrating towards southwest, consistent with across-divide χ contrasts, and may reflect
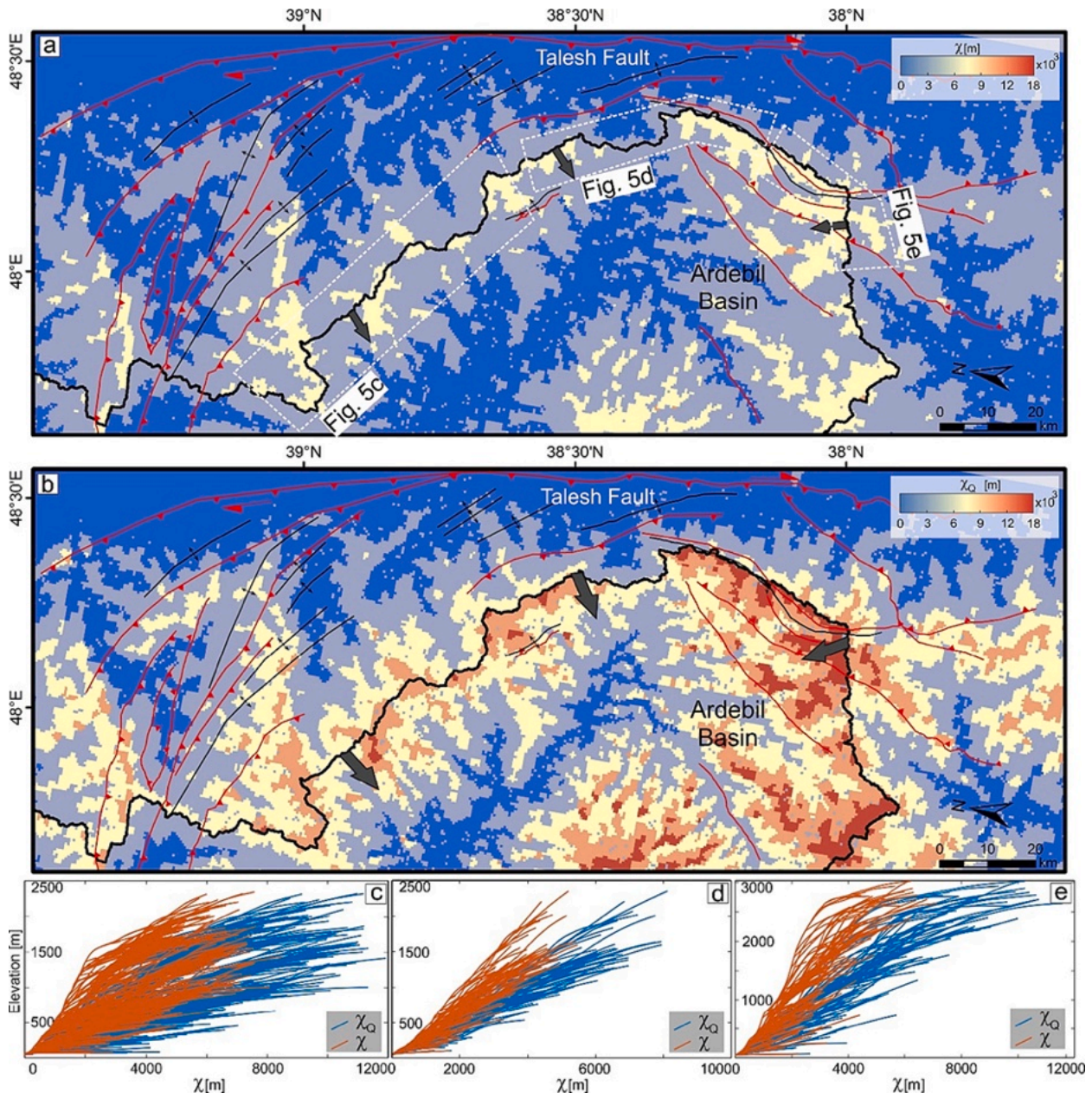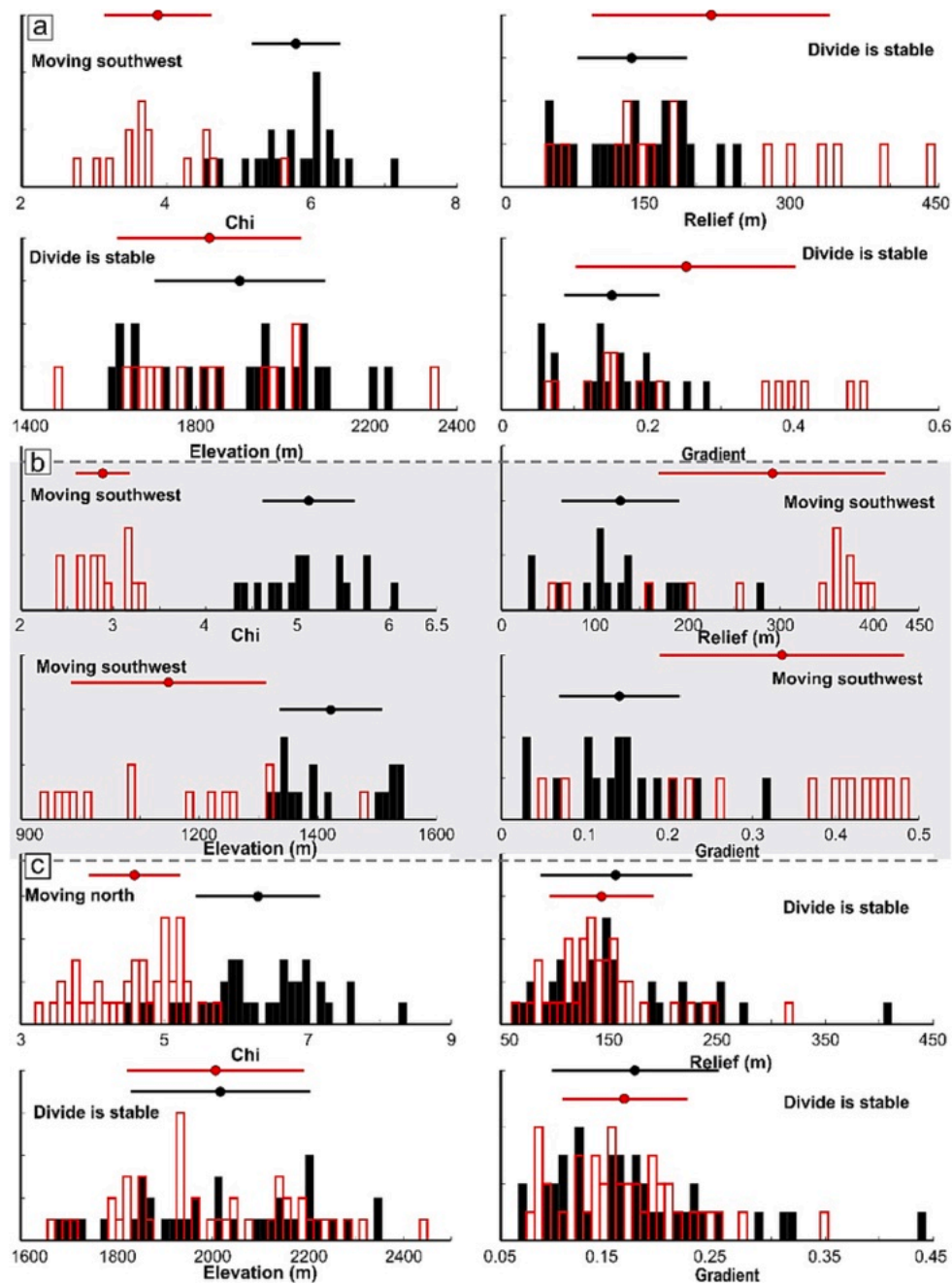

Fig. 5. Interpolated map of (a) χ and (b) χ_Q. Black arrows show the direction of the divide movement. (c), (d), and (e) Comparisons between χ-z (orange) and χ_Q-z (blue) profiles for catchments in the north, central, and southern parts of the range, respectively.

Fig. 6. Divide stability analysis of the study area. (a), (b), (c) Representative histograms of divide metrics for the ARD3, ARD6, and ARD14 segments, from the north, central, and southern sectors of the Ardebil Basin main drainage divide, respectively. Histograms with black rectangles exhibit watersheds in the interior of the plateau, while white histograms with red outlines show watersheds on the exterior of the plateau (towards Caspian Sea flank).

progressive capture by major rivers (Fig. 8).

The geometric properties of the divide suggest the existence of wind gaps, hillslope undercutting by rivers, and spatial anomalies in erosion rates, which based on Scherler and Schwanghart (2020) are diagnostic for past or ongoing mobility of drainage divides and could be interpreted as signatures reflecting mobile divides that tap into existing drainage networks. Accordingly, sharp-crested and shortened hillslopes, as well as beheaded streams were recognized in Google Earth images, supporting the divide mobility process in the direction of lower hillslope relief (Figs. S3d and S5).

Additionally, based on Forte and Whipple (2018), in a drainage divide the presence of a χ-anomaly along with the absence of a Gilbert anomaly, for instance segments ARD11 to ARD14, and to a less extent ARD2 and ARD3 (Fig. 7e), illuminates a spatial gradient in uplift rate

and/or erosional efficiency. The study of the steepness index, longitudinal, and χ-transformed river profiles provide insights for understanding the nature of these spatial gradients.

4.2. Stream network analysis

4.2.1. Steepness index (k_{sn})

The steepness of channels is generally dependent on uplift rate, erodibility of the rocks, and climate (e.g., Snyder et al., 2000; Kirby and Whipple, 2001; Kirby et al., 2003; Duvall et al., 2004; Kirby and Whipple, 2012; Miller et al., 2013; Adams et al., 2020; Leonard et al., 2023). Therefore, assuming similar rock erodibility and climate, by using k_{sn} and other geomorphic indices, regional rock uplift rate patterns can be identified. The streams located in the eastern flank of the Talesh
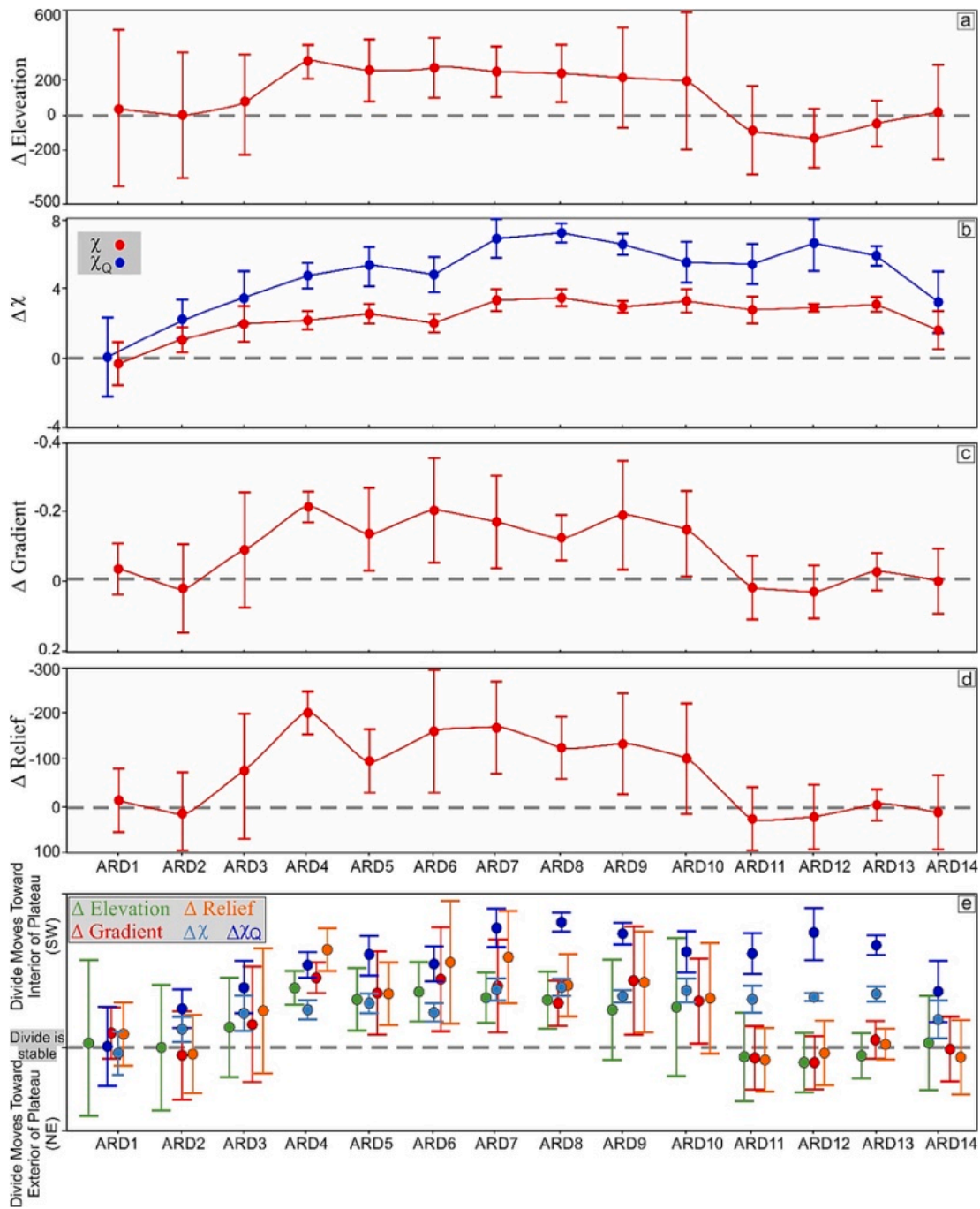
Fig. 7. Results of Gilbert metrics, χ and $χ_Q$ for the different drainage divide segments. (a), (b), (c), and (d) indicate the stability status and the potential divide mobility direction based on Δ elevation, $Δχ$ (red)- $Δχ_Q$ (blue), Δ gradient, and Δ relief, respectively for the 14 segments of the main divide. The grey dashed line shows the divide stability line. If the error bar determined by bootstrapping for a single divide segment touches the stability line, that segment is stable in that metric. Note that the y-axes of Δ relief and Δ gradient are reversed. Accordingly, the values above and below the divide stability lines suggest divide instability and movement towards the interior (mostly to the SW), and the exterior of the plateau, respectively. (e) Standardized delta plot for the 14 segments along the main drainage divide. Error bars represent standard deviation.

Mts. are dominantly in Eocene and Oligo-Miocene volcanic and volcaniclastic rocks, which are exposed to precipitation rates, ranging mostly from ~350 to 800 mm/yr (Fig. 2).

This part of the study area presents the highest k_{sn} and topographic slope values. Conversely, the lowest k_{sn} and slope values are observed in the Ardebil Basin in the interior of the plateau (Fig. 8a). The central and southern sectors of Talesh Mts. have higher HI (>0.5) and relief values (1200-2100 m) than the northern section indicating a greater variation in elevation.

4.2.2. Modified steepness by spatial rainfall variability (k_{snQ})

The complexity of tectonically active regions such as Talesh Mts. provides an excellent opportunity to see the patterns of k_{sn} and k_{snQ} (Leonard et al., 2023; Fig. 8) in understanding the fundamental mechanisms affecting landscape evolution. Accounting for variability in rainfall patterns amplifies the sensitivity of channel steepness to lithologic and tectonic controls on topography, thereby improving the accuracy of forecasts for erosion and rock uplift rates (Leonard et al., 2023). With similar uplift rate and rock type, catchments that

9
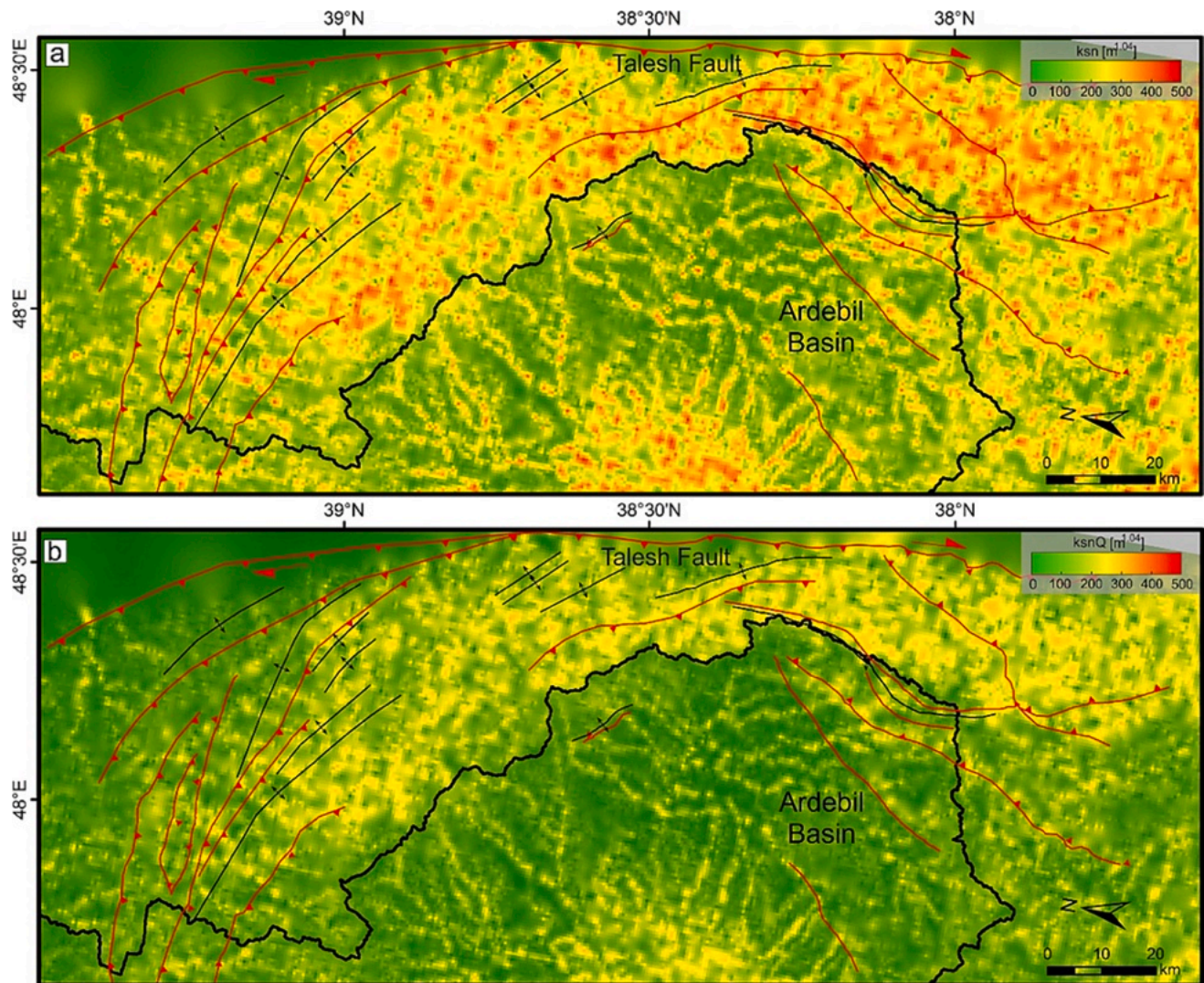
Fig. 8. Interpolated maps of (a) normalized steepness index (k_{sn}), and (b) k_{snQ}. Note that values are systematically higher along the eastern slope of the Talesh Mts.

experience greater amounts of precipitation are less steep than those with lower rainfall at steady state (Adams et al., 2020). In the study area, the pattern of k_{snQ} and χ_Q includes rainfall. Thus, k_{snQ} was used to isolate tectonic and lithologic elements and capture the impact of climate. The k_{snQ} values (Fig. 8b) are lower than the k_{sn} values by roughly two times, consistent with the differences in χ and χ_Q values (Fig. 5). This pattern is typical of regions with low rainfall. In the χ_Q plots (χ_Q -elevation), k_{snQ} is the slope of the profiles, thus, a higher χ_Q means that there are lower k_{snQ} values on average throughout the catchment than k_{sn} values.

Additionally, by comparing the steepness index and k_{snQ} (Fig. 8) a possible interpretation could be that contrasts in k_{snQ} are lower than k_{sn}. By comparing these two maps with the geological and precipitation maps, the high channel steepness index values do not seem to be completely correlated to the lithologic domains nor to the distribution of precipitation rates, although precipitation may have a limited contribution to the landscape evolution of the region.

4.2.3. Knickpoints and incision analysis

Knickpoints were extracted using *knickpointfinder* function in TopoToolbox (Schwanghart and Scherler, 2014; Schwanghart and Scherler, 2017) from the smoothed river profiles. For each river profile we calculated the tolerance value separately, which shows uncertainties that are inherent in longitudinal river profiles. This tolerance value is higher than the maximum expected error between the measured and the

true river profile. We used this uncertainty estimate derived from each river profile as direct input to *knickpointfinder* (Schwanghart and Scherler, 2017). Lithologic and non-lithological knickpoints were identified by comparing their spatial distribution with available geological maps, satellite images, and χ-elevation plots. Under uniform climate/ rock type, knickpoints representing transient adjustment to an increase in rock uplift rate should cluster around the same χ (Perron and Royden, 2013).

The non-lithological knickpoints are located on the slope break changes in the χ-transformed profiles (Figs. 9 and 10), but lithological knickpoints may also record information on transience. In this study, the transient analysis focuses on non-lithological knickpoints. In terms of elevation, the major non-lithological knickpoints in different parts of the study area are located between 1000- 1500 m, 600- 1200 m, 2000- 2750 m which reflect northern, central, and southern sectors, respectively (yellow stripes; Fig. 10a, c, e, and g), and clustered roughly at values of χ of 2000–4000. These knickpoints separate gentle upstream river segments from steep concave up downstream segments (different k_{sn} values; Fig. 10).

In the north, central, and southern sectors of the range, the high-standing relict landscape has a mean k_{sn} of 130 ± 4 m$^{1.04}$, 371 ± 7 m$^{1.04}$, and 236 ± 8 m$^{1.04}$ respectively (Fig. 10). While, for the landscape downstream of the non-lithological knickpoints in these sectors, the mean k_{sn} values are 620 ± 10 m$^{1.04}$, 414 ± 12 m$^{1.04}$, and 1020 ± 10
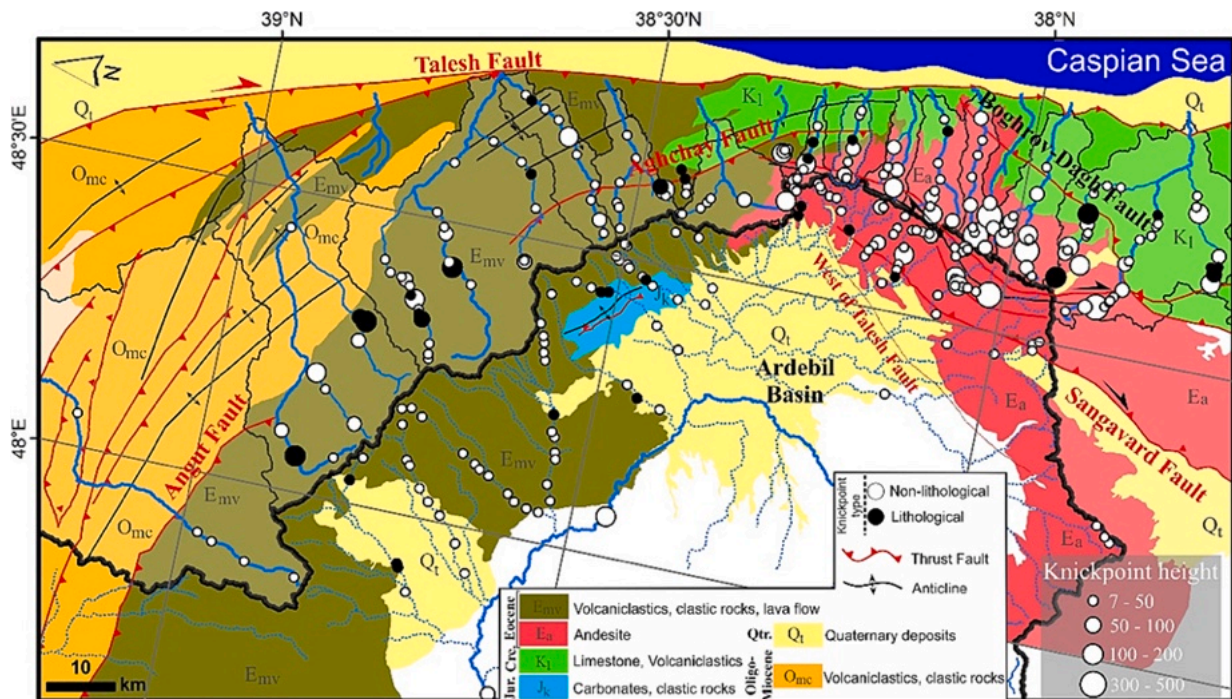
Fig. 9. Spatial distributions of knickpoints in the three sectors of the Talesh Mts. Lithological and non-lithological knickpoints with their heights are represented on the geological map of the study area. Field photos of the knickpoints in the Talesh Mts. can be found in the Google Maps Photos (source: http://earth.google.com).

m$^{1.04}$ (Fig. 10).

We used transient stream profiles to quantify the fluvial incision in the study area. By reconstructing the river profiles from the relict landscape (i.e., upstream of the highest non-lithological knickpoints; e. g., Clark et al., 2006; Schildgen et al., 2012; Miller et al., 2013; Calvet et al., 2015; Fox, 2019), the total magnitude of fluvial incision has been computed for each sector, in the north, central and southern parts of the mountain range.

The main transient stream profiles in the northern sector, yielded a mean fluvial incision of ~ 800 m, with maximum value of 2500 m. In the central sector, where most of the rivers appear to be near equilibrium, the mean magnitude of fluvial incision is only ~ 400 m, with a maximum value of 700 m (Fig. 11b). In the southern sector, rivers are characterized by strong disequilibrium profiles with high-standing non-lithological knickpoints lying at the margin of a low-topographic relief and delimiting segments with high k_{sn} from those with low k_{sn} values, in the downstream and upstream portion of the fluvial channel, respectively. Estimates of fluvial incision for the southern sector of the mountains based on main river profiles of the catchments is ~ 1600 m, which is the highest in the study area (Fig. 11).

4.3. Rock strength investigation

In order to determine the rock strength in different parts of the study area and to isolate the effect of rock type on erodibility, the mechanical strength of rocks has been measured. Our research provides a multi-faceted analysis of lithological characteristics (Table 1; Figs. 12, 13), which impacts the erodibility of bedrock, divide stability and knickpoint migration in the study area. The outcomes of rock strength and range of uniaxial compressive strengths by using Schmidt hammer are documented and displayed on the standard Schmidt diagram.

The Schmidt hammer results (Tables S1-S3) indicate that in the central Talesh Mts., the volcaniclastic units have the lowest UCS values (19–33 MPa) among the three sectors (Fig. 13b). Competent andesite-basalt in the north, and strong andesite in the south have the highest uniaxial compressive strength ranging from 63 to180 and from 47 to 135 MPa, respectively. Although UCS results from point-load tests are

compatible with Schmidt hammer results, the UCS range from point load tests is generally greater than that of ones obtained with the Schmidt hammer (Fig. 13c). This wide range of UCS values for the north, central, and southern sectors is 66–329, 16–97, and 29–169 MPa, respectively. To a large extent, the rock-type characteristics, and UCS values in the north and southern sectors are similar. The results of point load tests are presented in Tables S4-S6 (see the Supplementary materials). In a nutshell, all the results from Schmidt hammer, point-load test, and GSI (Fig. S6) in three different scales from rock matrix and rock mass to the entire outcrops were consistent with each other, and these erodibility proxies are all in agreement.

5. Discussion

5.1. Investigation of divide stability

Although χ and χ_Q maps suggest that the divide segments are dynamic and migrating towards the interior of the plateau (Fig. 5a), the Gilbert metrics indicate that the drainage divide in the northern and southern parts of the Talesh Mts. is static (Figs. 6 and 7). Thus, both χ map and Gilbert metrics suggest that the central sector of the drainage divide may be unstable and migrating to the southwest (i.e., to the plateau interior). Considering that instability of the divide segments denotes drainage area loss in the Ardebil Basin, these area changes should also result in stream power changes (e.g., Willett et al., 2014). Additionally, based on Forte and Whipple (2018), in a drainage divide the presence of a χ-anomaly along with the absence of a Gilbert anomaly, for instance segments ARD11 to ARD14, and to a less extent ARD2 and ARD3 (Fig. 7e), illuminates a spatial gradient in uplift rate and/or erosional efficiency. The study of the steepness index, longitudinal, and χ-transformed river profiles provide insights for understanding the nature of these spatial gradients. Since χ metric integrates the entire river catchment upstream from the base level and tells us about the erosion rate in the catchment scale, we can infer that the patterns of erosion and uplift rate may be higher in the eastern side of the divide in its entire segments towards the wet flank of the mountain range. One possible cause for the inconsistency between χ and Gilbert metrics' results in the
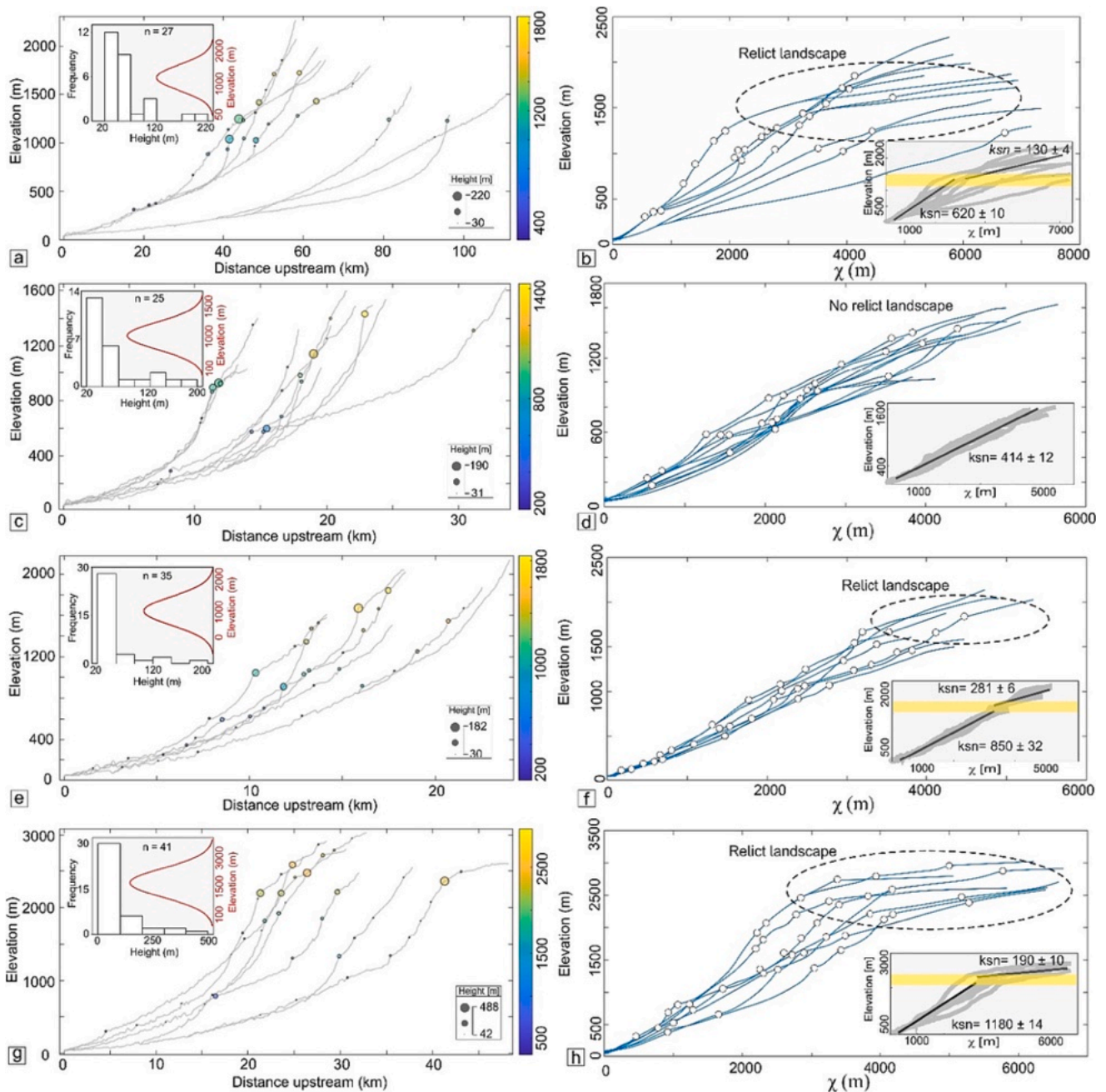
Fig. 10. Longitudinal profiles and χ-transformed plots with major knickpoints. (a-b) northern sector, subbasins 1 to 3; (c-d) central sector, subbasins 4 to 7; (e-f) southern sector, subbasins 8 to 10; (g-h) southeastern sector, subbasins 11 to 13 of the Talesh Mts. The inset plots in the χ profiles indicate the mean regional k_{sn} values upstream and downstream of the highest knickpoints. The inset histogram in the longitudinal profiles represents the frequency distribution of the elevation and height of the knickpoints.

northern and southern sectors of the mountain range is spatial variability of rock uplift and/or erosional efficiency, which perturbs the χ over the longer timescales (e.g., Forte and Whipple, 2018).

In the northern and southern sectors of the Talesh Mts, the divide segments are stable and virtually near the topographic crest of the range. Conversely, the segments in the central part are migrating southwest towards the low-relief side. This may represent contrasting erosion rates across the divide which are reflected in the potential movement of these divide segments towards the interior of the plateau. The topography of the region, as indicated by agreement between all topographic metrics, suggests that divide instability in this part of the study area is due to piracy of the plateau rivers (Fig. 14). Due to piracy and headward erosion, the headwaters of the rivers got captured. The headwaters of

the modern rivers (yellow color; Fig. 14b-d) who were flowing towards the interior of the plateau before the asymmetric uplift, are now flowing in the opposite direction to Caspian Sea due to divide mobility and capturing (Fig. 14).

In the northern and southern parts of the range, the erosional wave related to the most recent uplift pulses has not reached the divide yet. Therefore, these sectors indicate symmetry and steady-state by the Gilbert metrics, since these metrics are measured locally at the divide and solely gives us information about the local erosion rates, and they may not detect far field influences that drive the long-term evolution. On the other hand, in the central part, the erosional wave reached the divide moving it towards southwest, as testified by Gilbert metrics which suggest asymmetry. In this sector, a limited contribution of the annual
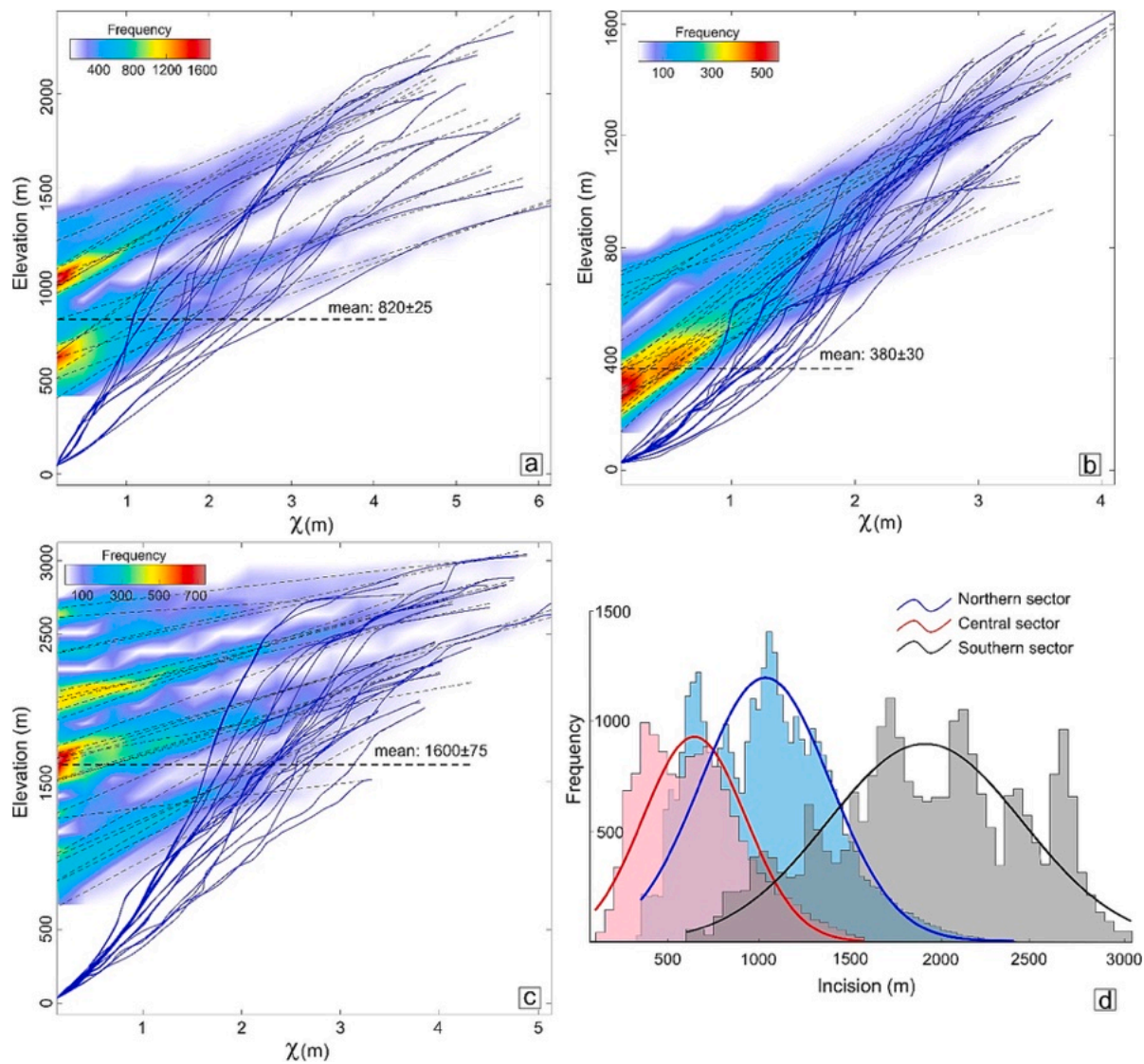
Fig. 11. Modern longitudinal profiles and projections of the relict landscape in (a) north, (b) central, and (c) southern sectors of the range. The profile is constructed using the relict landscape, upstream of the major and highest knickpoints. (d) Histograms and frequency diagrams of magnitude of incision in the three sectors of the mountain range.

Table 1
Rock-type characteristics, and uniaxial compressive strength of rocks in the north, central, and south of the Talesh Mountains.

Mountain sectors	Schmidt hammer value	Uniaxial compressive strength	Point load value (KN)	UCS (point-load)	Erodibility	Rock characteristics
Northern part	20–60	63–180	13–42	66–329	Very resistant	Very strong and competent igneous rocks. Andesite-basalt, breccia tuff, andesitic massive lithic tuff
Central part	5–34	19–33	2–14	16–97	Very erodible	Weak to very weak rock- crumbles with hammer blows. Igneous rocks; highly weathered and weakly compacted sedimentary rocks: Tuff, pyroclastics with volcanic clasts (andesite and basalt)
Southern part	20–54	47–135	7–44	29–169	Resistant	Very strong rock- hard to break with hammer. Moderately weathered and fractured. Competent igneous rocks: Porphyritic andesite, andesitic basalt

precipitation can be taken into consideration, since in the central sector it is more contrasting across the divide.

Generally, we can infer the progressive motion of the divide in the central sector due to reaching of the erosional wave to the divide. While at longer- wavelength and timescale, the main divide in all the three sectors is mobile (as suggested by χ) due to higher erosion/uplift rates in the wet flank of the Talesh Mts.

Thus, the erosional exhumation (Madanipour, 2023) due to higher

precipitation (Figs. 3b, and 16c) and/or difference in the rock strength (Figs. 12, and 13) can be introduced as the main driver of transient landscape in the central sector. In the following paragraphs we discuss the role of each factor thoroughly.

5.2. Topographic and structural features of the study area

The Talesh Mts., bounded by the Talesh Fault to the east, represent a

Fig. 12. Field photos showing the lithological units in the study area. (a) In the northern sector, resistant competent andesite, andesite-basalt, and volcaniclastic units are exposed. (b), (c) Close-up view of the rock units in the north of Talesh Mts. (d-f) In the central sector, pyroclastic, and week rock units are common, and variations in rock strength and weathering intensity exist. In this part due to higher precipitation, the vegetation cover is greater than in the north and southern sectors. (g-i) Eocene weathered andesite exposed in the southern sector with several joint systems and fractures. Roads and houses in all photos are for scale.

complex zone in terms of tectonic structures and surface processes. To decipher the signal of the inherited topography linked to the uplift history and long-term fault activity, we constructed three across and one along-divide swath profiles (Figs. 3b and 15).

Along the main drainage divide, in the northern Talesh Mts., the values of local relief are low, and characterized by low incision values. On the other hand, in central Talesh Mts. the high values of local relief document higher incision/uplift of the mountain range (Fig. 15a), and mean elevation approaches the maximum elevation which could reflect a transient adjustment to higher uplift rates (e.g., Keller and Pinter, 2002; Wobus et al., 2006b; Pérez-Peña et al., 2017).

In the central Talesh Mts, Hi values are between 0.5 and 0.75, which indicate mean elevations close to maximum elevations and, consequently suggest the occurrence of a young transient landscape (Fig. 15a). Conversely, lower values of hypsometric integral in the northern and southern parts of the mountain indicate a mature landscape whose mean elevation is closer to the minimum, indicating that these parts of the divide have not yet experienced the erosional wave, or the erosional efficiency in these parts is considerably lower than the central part, which is in agreement with the position of knickpoints.

In the along-strike P1 swath profile, the average variation between the maximum and minimum curves in the northern Talesh Mts. is very low (500- 1000 m). In the central Talesh Mts. the variation is about 1400–2000 m, which is the highest value of the entire study area. Swath profiles indicate that the highest elevations and local relief (1200–2100 m) values are in the central and southern sectors of the range. These

anomalies correlate with the highest values of DAI (Divide Asymmetry Index) (see the Supplementary materials) and the hypsometric index in the study area (Fig. 15a). The analysis of the swath profiles suggests that uplift rates along the mountain range are not uniform which is consistent with other metrics/analysis (e.g., χ, k_{sn}, knickpoints, etc). Perpendicular to the general trend of the main divide (swath P1; Fig. 15a), topographic variations at the north, central, and southern parts of the Talesh Mts. (swaths P2, P3, P4; Fig. 15b-d, respectively) have been evaluated. In swath P2, the values of local relief and hypsometric integral are low in the west side of the main divide (plateau interior) and increase towards the east in the middle of the profile (Fig. 15b), where the Ojagh-Gheshlagh anticline with a convex crest presents high local relief. In the central Talesh Mts., in swath P3 (Fig. 15c), adjacent to the divide point, there is an abrupt increase in hypsometric integral (THi*) from 0.25 to 0.6.

Additionally, the local relief increases from 350 to 1000 m. In the middle of the profile, in the anticline located in the footwall of the Aghchay Fault, local relief value increases. The southern sector of the Talesh Mts. reaches the highest elevation of the study area (maximum elevation of 3300 m). In this section, the range of local relief values are lower than those in the northern, and central parts, and most of the high values correlate with the location of the main faults (swath P4; Fig. 15d).

The distribution of k_{sn} and hillslope gradient of the study area are plotted in both east and west side of the main divide in order to reveal the asymmetric uplift (Fig. 16). Generally, the normalized channel steepness values decrease from east to west orthogonal to the main
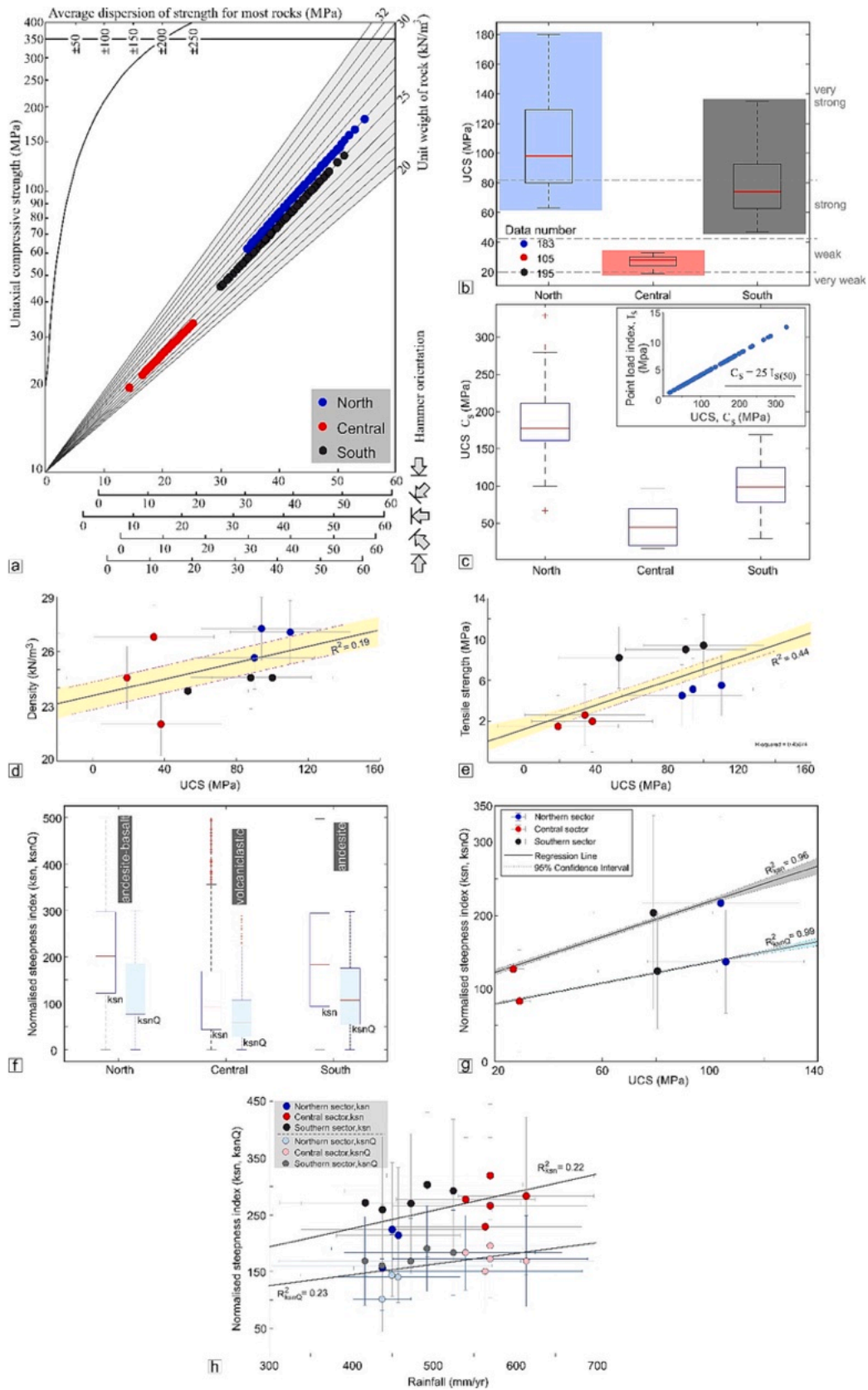
(caption on next page)

Fig. 13. Comparison between Schmidt hammer and point load test, and k_{sn}- k_{snQ} with mechanical rock strength and precipitation. See the main text and Supplementary materials for details, and conversion of Schmidt hammer rebound values and Point Load Index values ($I_{s(50)}$) into uniaxial compressive strength (UCS). (a) Rebound data in each sector plotted on the Schmidt hammer chart. (b) and (c) Boxplots of rock strength and range of uniaxial compressive strengths in the north, central, and southern sectors by using Schmidt hammer and point load test, respectively. The inset in (c) upper right, reports the relationship between Point Load strength index and uniaxial compressive strength. The median is represented by a red line within each box. Box extent illustrates the interquartile range, and whiskers represent minimum and maximum values. (d) and (e) Relation between rock properties (mainly density) and tensile strength of the sampled rocks as a function of uniaxial compressive strength, respectively. (f) Average and standard deviation of k_{sn} and k_{snQ} in the three sectors of the mountain range for each lithological unit. (g) Linear regression values of k_{sn} and k_{snQ} versus UCS for each lithological unit. (h) Relationship and correlation between k_{sn}, k_{snQ} average values in the uplifted relict landscape and precipitation.
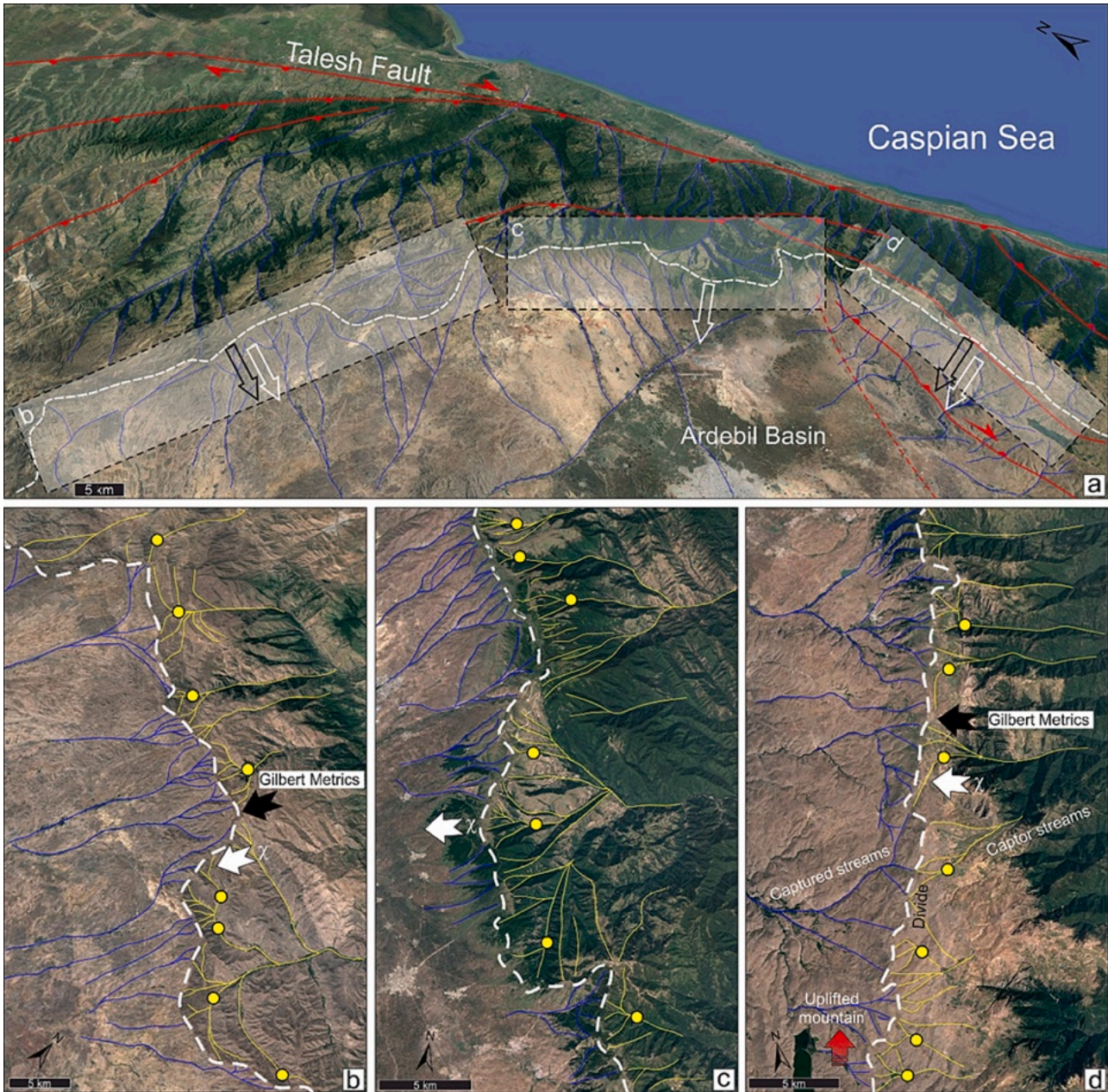

Fig. 14. Drainage pattern evolution and channel configuration in the NW sector of the Iranian plateau. (a) Google earth image of the study area showing the position of the main divide with river networks. (b), (c), and (d) the evidence of river piracy and wind gaps in the north, central, and southern sector, respectively. Note the strong topographic asymmetry across the divide and the orographic effect on precipitation as indicated by the vegetation pattern. White dashed line indicates the main drainage divide. Yellow circles show the locations of elbow of captures. White and black arrows illustrate the predicted divide mobility by χ and Gilbert metrics, respectively.

divide (Figs. 9 and 15), and they are markedly higher across the Talesh Mts. than that of the Ardebil Basin. Therefore, it can be concluded that the study area has likely experienced an asymmetric uplift pattern (Moumeni et al., 2022), with higher uplift rate on the eastern side of the divide and the mountain range (towards the Caspian Sea wet flank). Consequently, the topography in the eastern side of the main divide is
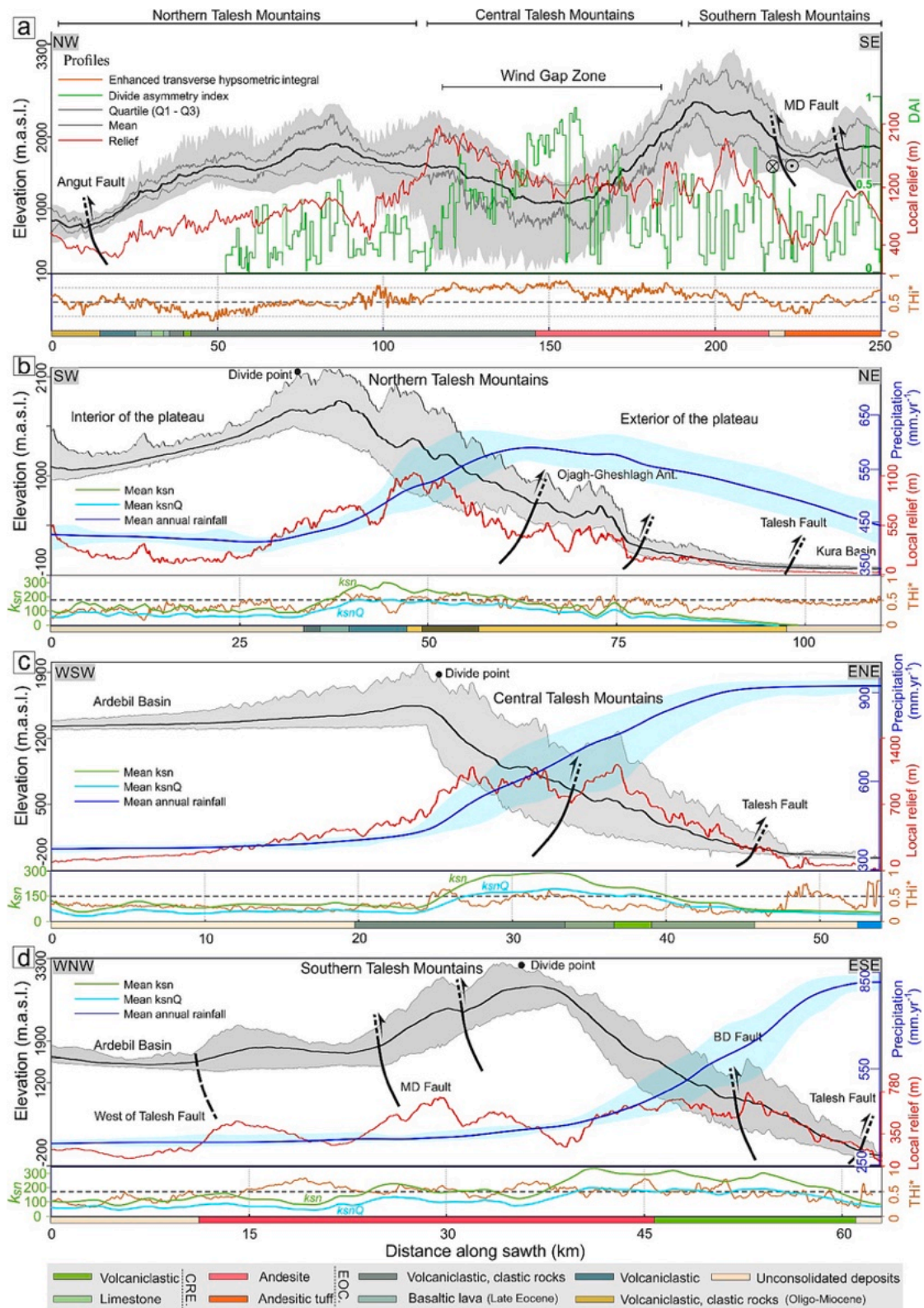
Fig. 15. (a) Along (P1), and (b-d) across strike (P2 to P4) swath profiles of the Talesh Mountains. The swaths present a strong asymmetric topography and orographic precipitation across the main divide. In each profile, local relief (red lines), enhanced transverse hypsometric integral (Thi*; orange lines), steepness index values (k_{sn}; light green lines), k_{snQ} metric (light blue lines), and the precipitation rate (thick dark blue lines) are represented. In the swath P1 (a), divide asymmetry index (DAI) profile is illustrated with green color. Swath window is 20-km-wide. Location of the swaths are shown in Fig. 3b, and S3b. In P2 to P4 swath profiles, the base level in the interior (left side of the swath) and exterior of the plateau (right side of the swath) is fixed at 40 m. Note that in these profiles the base level in the interior of the plateau is not represented.
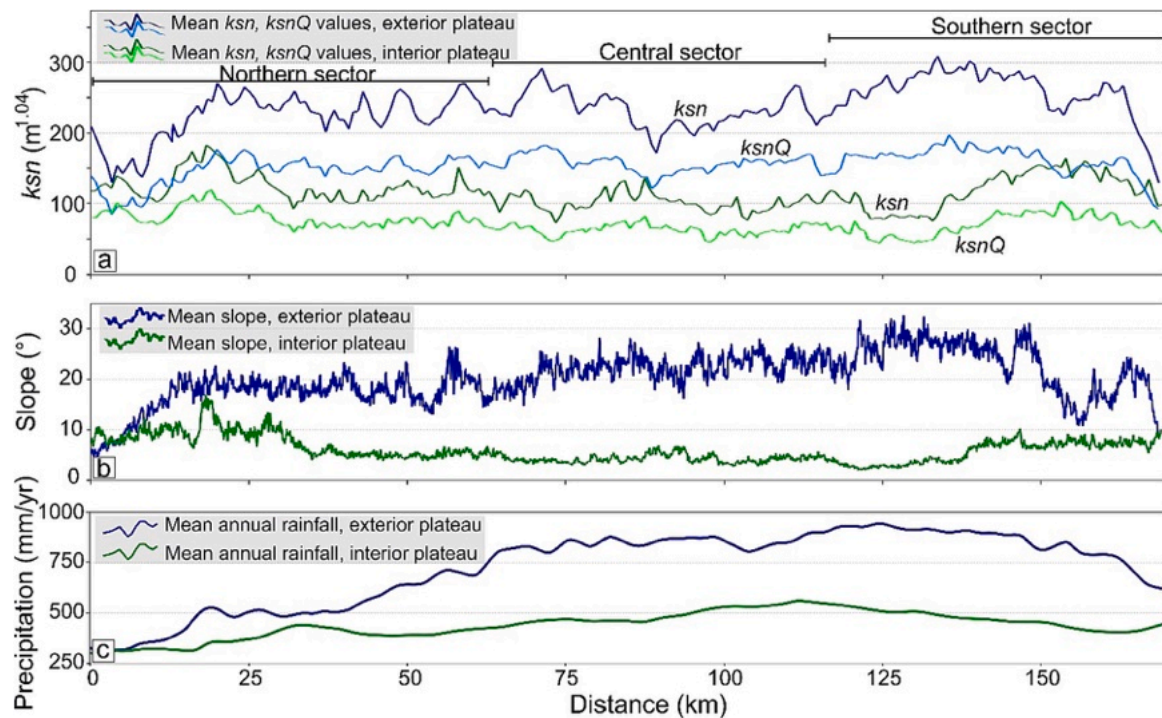
Fig. 16. Profiles of the mean values of steepness index, gradient, and annual precipitation. (a), (b), and (c) Comparison of the k_{sn}- k_{snQ}, slope degree, and annual rainfall mean values between the two along the main drainage divide of the Ardebil Basin, respectively in the interior and exterior (towards the wet flank of the range) of the plateau.

steeper than that of in the western side. Thus, the higher k_{sn} testifies that topography in the exterior plateau has already adjusted to uplift rates with respect to the interior plateau (Figs. 16b, and S3c).

5.3. Transient topography and asymmetric uplift

The asymmetric uplift scenario agrees with accelerated middle Miocene exhumation at ~12 Ma as constrained by U-Th/He thermochronometric data along the thrust and reverse faults in the northern and southern Talesh Mts., and the limited exhumation in the central part (Madanipour et al., 2017). The thrust kinematics has been proposed for the faults in the Talesh Mts. during early Oligocene - middle Miocene when the regional convergence direction was towards northeast. In middle Miocene, due to a change in the regional convergence direction towards north, the strike-slip component became dominant in the central part of the Talesh Mts. (Madanipour et al., 2013, 2017 and 2018). Furthermore, GPS data suggest for the northern part of the range a minor component of NNE-SSW extension perpendicular to the mountains belt at a rate < 2 mm/yr. At the same time, for the southern and central parts of the Talesh Mts., 5–6 mm/yr of horizontal shortening and 4–5 mm/yr of right-lateral strike-slip movements have been documented (e.g., Djamour et al., 2011; Madanipour et al., 2018). Hence, the Talesh Fault can be considered the main structure of the margin of the Iranian plateau, which controls rock uplift and caused asymmetric uplift of the Talesh Mts. Furthermore, several wind/water gaps, beheaded valleys, abandoned, and relict channels have been recognized by remote sensing studies (Fig. 14) suggesting a drainage reorganization following a asymmetric uplift, and/or erosion patterns.

The stability of the main drainage divides at the topographic crest of a mountain in the presence of homogeneous tectonic uplift, rock erodibility and precipitation rate, could be disturbed when the mountain experiences asymmetric uplift. Consequently, the main drainage divide will migrate towards the high-uplift side till it reaches a steady-state (e. g., Forte and Whipple, 2018; He et al., 2021). Furthermore, in response to an asymmetric uplift, the divide movement direction could be from

the high-uplift side towards the geometric center of the mountain to achieve a new steady-state (Ye et al., 2022). The strong variation in the normalized channel steepness index, topographic slope, elevation, and fluvial incision between the portions of the landscape downstream and upstream of the highest non-lithological knickpoints documents a transient condition of the Talesh Mts. topography. This transient state could be attributed to several processes, such as drainage reorganization, climate change, bedrock erodibility, eustatic sea level fall and tectonic uplift (e.g., Hancock and Kirwan, 2007; Kirby and Whipple, 2012; Miller et al., 2013; Ballato et al., 2015). In this study, drainage reorganization due to tectonic uplift and erosion appear to be the main cause of this transient state since there is evidence of knickpoints, and wind gaps related to river piracy processes (Fig. 14).

An increase in erosion rates due to climate variations (i.e., increase in precipitation rates) is also likely, and may have acted as an additional factor enhancing the divide mobility. The abrupt break in the river longitudinal profiles and χ-z plots at the highest non-lithological knickpoints and the position of the knickpoints in the χ space (Fig. 10b, d, f, and h) show that the two portions of the landscape upstream and downstream of these knickpoints erode at different rates (Schildgen et al., 2012; Miller et al., 2013; Olivetti et al., 2016; Clementucci et al., 2022). This is consistent with an increase in erosion and rock uplift rates propagating from the river outlet to the uppermost river segments (Miller et al., 2013; Gallen and Wegmann, 2017; Racano et al., 2021, 2023). Consequently, the highest knickpoints represent a response of the fluvial system to an increase in rock uplift rates and hence mark a phase of topographic rejuvenation, while the uplifted relict landscape records the previous erosional conditions predating such an increase. Conversely, the minor and non-lithological knickpoints located in the lower segments of the fluvial network, at 200–800 m and 400–1500 m in the north, central, and southern sectors, respectively, can be attributed to a Quaternary climate forcing (e.g., Hancock and Kirwan, 2007; Clementucci et al., 2023). This pattern of knickpoints is spatially consistent and does not show any channel steepness variation across the knickpoints in the longitudinal profiles and the χ-z plot (Fig. 10b, d, f,

and h). The present geomorphic configuration and high elevation of the study area is caused by the interplay of internal and external forces in different temporal scales. In this matter, three phases of Cenozoic deformation were documented in the Talesh Mts. Based on thermochronometry data (zircon bedrock U-Th/He ages), exhumation started in the late Oligocene (~27–23 Ma) and then accelerated in the middle Miocene (~12 Ma) and the early Pliocene (5 Ma). The last deformation phase resulted in exhumation along the thrust, reverse and strike-slip faults, which shaped the present-day architecture of the Talesh Mts. The late Oligocene phase (phase 1) which is recorded across the entire mountain range, caused shortening that was accommodated along reactivated and/or newly initiated thrust faults including the Sangavard, Boghrov-Dagh, and Angut faults. While the middle Miocene (phase 2) and early Pliocene (phase 3) phases are solely recorded in the northern and southern parts of the Talesh Mts. (Madanipour et al., 2017). Therefore, after phase 1, when the whole range uplifted, just the north and southern parts of mountains were uplifted during phase 2 and 3, while, in the central part without any significant tectonic activity, the erosion was shaping the landscape, and decayed the topography. In the northern and southern parts, although the divide is suggested to be stable by the Gilbert metrics, divide mobility towards the interior of the plateau should occur once the erosional wave reaches the present divide position as also suggested by χ. The reason for such a stability is related to the erosional wave in the northern and southern parts of the Talesh Mts. that has not reached yet the divide after the latest uplift phases. Thus, in these parts, the strength of the bedrock (Fig. 13) and the rate of precipitation (Figs. 3b, and 15) is lower which promote lower impact of surface processes and erosional dynamics than the central part of the range.

5.4. Climate variability and influence of orographic precipitation

Several studies have shown the mechanism and limitations of across-divide χ metric to assess the direction and rate of a migrating divide and interpret their spatial patterns in connection with tectonic forcing (e.g., Willett et al., 2014; Yang et al., 2015; Forte and Whipple, 2018; Winterberg and Willett, 2019; Su et al., 2020; Maneerat and Bürgmann, 2022). Across divide differences in χ may reflect differences in erosion rate and divide motion if rock uplift, rock erodibility, and climate are uniform. If the assumptions of uniform conditions inherent are not met, χ-anomalies may occur even if the divides are stable, and hence χ map may suggest incorrect divide movement (e.g., Willett et al., 2014; Whipple et al., 2017; Forte and Whipple, 2018).

The impacts of weathering processes on erodibility and its variation in different parts of the mountain can be taken into consideration as an additional significant factor on the relative importance of rock strength (e.g., Shobe et al., 2017; Chilton and Spotila, 2022). Although the properties of rocks can considerably impact landscapes, this influence may not always be the most prominent factor. Therefore, the contrast in rock strength needs to be evaluated in relation to the magnitude of tectonic or climatic variation (Mitchell and Forte, 2023). Mountainous terrains commonly experience orographic precipitation patterns. Hence, if the erosion mechanisms in such landscapes are responsive to temporal or spatial fluctuations in rainfall, alterations in orographic precipitation patterns can significantly impact the mountain landscape evolution (Roe, 2005; Leonard and Whipple, 2021).

High elevations in the north and southern sectors receive approximately 400–500, and 500–900 mm/year, respectively. Whereas the central sector experiences ~800–1100 mm/year of rainfall (Figs. 3b, and 16c). The study area covers over 200 km along strike and includes tectonically activity region with variable lithologies that experienced several deformation episodes in the Cenozoic (Eocene, Miocene, Pliocene), alongside climatic fluctuations. The k_{sn} and k_{snQ} metrics reflect erosion rate patterns, and k_{snQ} gives the best remote estimate of spatial variations in erosion at the landscape scale as it accounts for precipitation (Leonard et al., 2023). Since k_{sn} fails to account for the distribution

of precipitation, it forecasts higher erosion rates in the study area compared to k_{snQ}. The main divide effectively separates the zones where k_{sn} and k_{snQ} forecast higher erosion rates.

In the study area, basins with higher precipitation rate show higher values of steepness. These basins will reach equilibrium more rapidly and exhibit higher rates of erosion over time during the process of landscape adjustment, compared to basins that receive lower levels of precipitation (Ferrier et al., 2013). Furthermore, some catchments in the region with similar lithology, such as andesite and volcanoclastic rocks, that undergo contrasting rainfall, have identical k_{snQ} values, suggesting that rock uplift rates must be identical.

Therefore, the difference between k_{sn} and k_{snQ} suggests different spatial patterns of uplift/erosion rates. This difference between the two metrics highlights the erosion rate patterns in the study area. Across the main divide boundary in the south and northern parts, the precipitation rates are rather similar, while in the central parts, where the precipitation appears to be higher on the eastern flank, there is not that much difference in the k_{sn} values. Thus, precipitation is not a major factor affecting the geomorphic indices and does not dominate the topographic expression of the range, although it represents a potential factor controlling the topographic evolution of the study area. Hence, it seems that tectonic rock uplift/erosion rates govern the drainage evolution in the study area.

Additionally, in the central Talesh Mts., the rapid incision of the rivers may be caused by Caspian Sea base level fall which led to the onset of erosional exhumation in the eastern wet flank of the Talesh Mts. at ~5.6 Ma (e.g., Ballato et al., 2015; Madanipour, 2023).

5.5. Bedrock erodibility and landscape response time

In landscape evolution processes, in addition to climate and tectonics, bedrock erodibility and rock strength play an important role. In fact, heterogeneous exhumation of strong and weak bedrock units can repress and intensify erosion respectively (e.g., Allen et al., 2013; Giachetta et al., 2014; Forte et al., 2016; Gallen, 2018; Campforts et al., 2020; Zondervan et al., 2020a) and critically influence the development of localized topographic relief. Therefore, it is necessary to understand the effects of erodibility when interpreting landscape processes and patterns. Difference in landscape response time to tectonic perturbations is a function of different factors including erodibility (Zondervan et al., 2020a), precipitation, drainage area, etc.

Our field observations and measurements have shown the influence of bedrock strength on the landscape of the region (Fig. 13). There may be substantial variations in the time it takes for fluvial and landscape systems to respond to tectonic disturbances. The northern and southern sectors are mostly characterized by transient river longitudinal profiles (Fig. 10b, and h). In general, 287 knickpoints have been recognized, which 34 of them are lithological knickpoints with a mean height of 50. The highest non-lithological knickpoints' heights in the north and southern sectors of the mountains are 120 m and 498 m respectively. In these areas the upstream segments are chiefly rectilinear with equilibrium profiles and are represented as straight segments in the χ space (Fig. 10). The southern sector has the highest non-lithological knickpoints for the entire study area (six knickpoints with a height of 120–200 m, and three knickpoints with a height of 300- 500 m).

On the other hand, in the central sector, most of the river profiles are equilibrated, with a mean k_{sn} value of ~350. Altogether, the distribution of the highest knickpoints and the estimated values of fluvial incision (Fig. 11) indicate the concentration of high incision in the south and north of Talesh Mts. This is also correlated with a regional increase in k_{sn} values downstream of the major knickpoints. Furthermore, the concentration of high k_{sn} values specifically in the southern section, where also weaker rocks crop out with respect to the northern part, supports higher rates of uplift and/or erosion in these parts of the study area.

Based on Zondervan et al. (2020a), the erodibility of bedrock greatly influences the expression of knickpoints in the landscape. Consequently,

when searching for tectonic signals in the landscape to investigate the histories of faulting, the effect of varying bedrock erodibility should be considered, and the strength of bedrock strongly controls the timescale over which such signals propagate upstream (e.g., Forte et al., 2016; DiBiase et al., 2018). In the central part of the study area, due to more erodible bedrock and maybe higher erosion, the propagation of knickpoints to the headwaters probably had been tens of kilometers within a relatively short time, and the lack of relict landscape in this sector does not allow us to constrain the magnitude of incision properly, that is why the estimated fluvial incision in this sector was the lowest all over the study area. Therefore, limited evidence in the river longitudinal profiles for tectonic perturbation is visible today. In contrast, in the north and southern sectors the presence of the resistant bedrock slows the migration of the wave of incision due to the initiation of the active reverse faults, and therefore, knickpoints are prominent in the river profiles. Furthermore, the effect of higher rainfall in the central part has increased the along-stream migration rate (celerity) of knickpoints, whereas the vertical rate and thus adjustment timescale is set by the uplift rate. Consequently, the lack of relict landscape in the central sector prevents us from estimating the minimum value of fluvial incision/rock uplift. The amount of fluvial incision should be greater than the southern and northern sectors because the relict landscape has been already eroded away by fluvial processes.

The rate of uplift/incision calculated here represents the minimum magnitude of rock uplift, since the Caspian Sea as the base level for all the rivers in the region has experienced several base level changes during the Late Cenozoic which was driven by the climate, tectonic processes, and the onset of subduction in the northern margin of the SCB (e.g., Axen et al., 2001; Allen et al., 2002; Forte and Cowgill, 2013; Ballato et al., 2015; Madanipour, 2023).

5.6. Erodibility-induced drainage divide mobility

In this study, it is anticipated that bedrock erodibility has a role in driving the mobility of drainage divide. Measuring and defining the erodibility of bedrock and the dynamics of drainage divide continue to be a significant issue. To tackle this problem, a comprehensive set of data on rock erodibility must be integrated with topographic measurements of the mobility of drainage divide in a mountain range (Bursztyn et al., 2015; Forte and Whipple, 2018; Zondervan et al., 2020b). In an active mountain belt like the Talesh Mts., the effect of lithologically-induced divide instability could be more complex. By combining assessments of variations in the erodibility of different rock types with geomorphic indicators of the movement of the drainage divide, we suggest a framework for the mobility of drainage divide caused by lithology, and higher erosional efficiency during the topographic growth of the Talesh Mts. range.

The lithological units in the study area generally consist of Eocene andesite, andesitic basalt, volcaniclastics in the northern, volcano-clastic- clastic rocks in the central, and andesite in the southern of Talesh Mts. (Fig. 3a). The specific characteristics of the lithological units across various sectors of the range are represented in Table 1. It seems that the higher density of rock joints and fractures in the south, with more precipitation and higher weathering rate is responsible for the lower rock strength in comparison to the northern sector. In the context of rock strength, we also considered the horizontal movement of contact of hard and soft rock units which can enhance drainage divide mobility. Based on Mitchell and Forte (2023), topographic advection is defined as the horizontal component of changes in topography related to the horizontal component of rock uplift, which can have a profound impact on convergent orogens, such as Talesh Mts. Therefore, pronounced transient responses within landscapes can be induced by the combination of horizontal tectonic displacements and variations in erodibility.

In the northern sector of the Talesh Mountains, the equilibrated landscape developed in a strong lithology that might be subjected to topographic advection. In the central sector, the dipping contact of

pyroclastic units and andesite (Fig. 12d) has caused the faster migration of the divide through the landscape respect to the northern and southern parts. Thus, the central sector may have experienced horizontal rock motion, which would create topographic advection that has led to present landscape asymmetry (Figs. 15c and 17). Topographic advection leads to the displacement of the primary drainage in the direction of advection (He et al., 2021; Mitchell and Forte, 2023) towards the interior of the plateau. The weaker lithology in this sector accompanied with higher precipitation rate (relative to the other sectors) can cause the movement of the drainage divide (Fig. 17). Moreover, the contact of weak and strong rocks can be raised by rock uplift and shifted horizontally by topographic advection (e.g., Mitchell and Forte, 2023). The lithological condition of the southern sector of the range is roughly the same as the northern sector. The results show that the equilibrated landscape formed in a strong lithology.

As we mentioned earlier, apart from tectonic uplift, spatial variation in bedrock resistance affects the erodibility coefficient and k_{sn} (e.g., Mills, 2003; Whipple, 2004; Clementucci et al., 2022). In particular, topographic relief and bedrock erosion may potentially be influenced by spatial variation in precipitation. The lack of any strong relationship between k_{sn}, k_{snQ} and rainfall (Fig. 13h) is consistent with variable rock type (erodibility) and/or uplift rates since the study area is not at steady state. We observed that resistant lithological units in the study area have higher k_{sn} average and UCS values on the relict landscape (Fig. 13f, g). Thus, we can conclude that various rock resistance and erodibility play a major role in the growth and decay of topographic relief when tectonic uplift is evenly distributed. Conversely, we know that the topographic evolution in regions undergoing active deformation can be significantly influenced by the horizontal motion of rocks and the resulting advection of the topography, it is still important to consider the role of tectonic deformation since it can cause such regions to contain rocks with varying strengths (e.g., Willett et al., 2001; Sinclair et al., 2017; He et al., 2021; Mitchell and Forte, 2023). Thus, the presence of horizontal rock motion, a common characteristic of tectonically active regions, may contribute to landscape transience resulting from differences in rock strength. Although, distinguishing this effect from those resulting from tectonic or geodynamic processes would still pose a considerable challenge (Mitchell and Forte, 2023).

Thus, besides the role of topographic advection which can function as another factor of transmitting transient signals across landscapes (Mitchell and Forte, 2023), uplift and exhumation of the Talesh Mts. (Fig. 17) associated with the regional deformation due to the initial and final Arabia-Eurasia collision and subsequent structural reorganization in the early Oligocene, middle Miocene and early Pliocene (Madanipour et al., 2017), should be noted as the primary main cause predating such factors we mentioned in this paper.

6. Conclusion

The possible scenario for the whole divide's behavior of the Talesh Mts. Range is associated with the contrasting erosion rates across the divide. The efficiency of erosion is primarily determined by the precipitation and the strength of exposed rocks. We can infer that divide is unstable in the study area in response to the asymmetric uplift and spatial variability of erodibility. Therefore, the divide instability in the NW of Iranian plateau is chiefly controlled by topography, especially slope and local topographic relief. While the precipitation rate has potentially been assisting, and magnifying the divide mobility, reorganization of river networks and landscape transience. Our findings represent that climate does not exert a first order and strong control on topographic growth and erosional efficiency in the study area.

The Ardebil Basin main divide continues to migrate towards the interior of the plateau. This movement will continue until these segments reach a steady-state, or uplift/erosion rate becomes uniform again. Accordingly, the results show the presence of a localized uplift gradient along the divide that is holding the divide in place in the
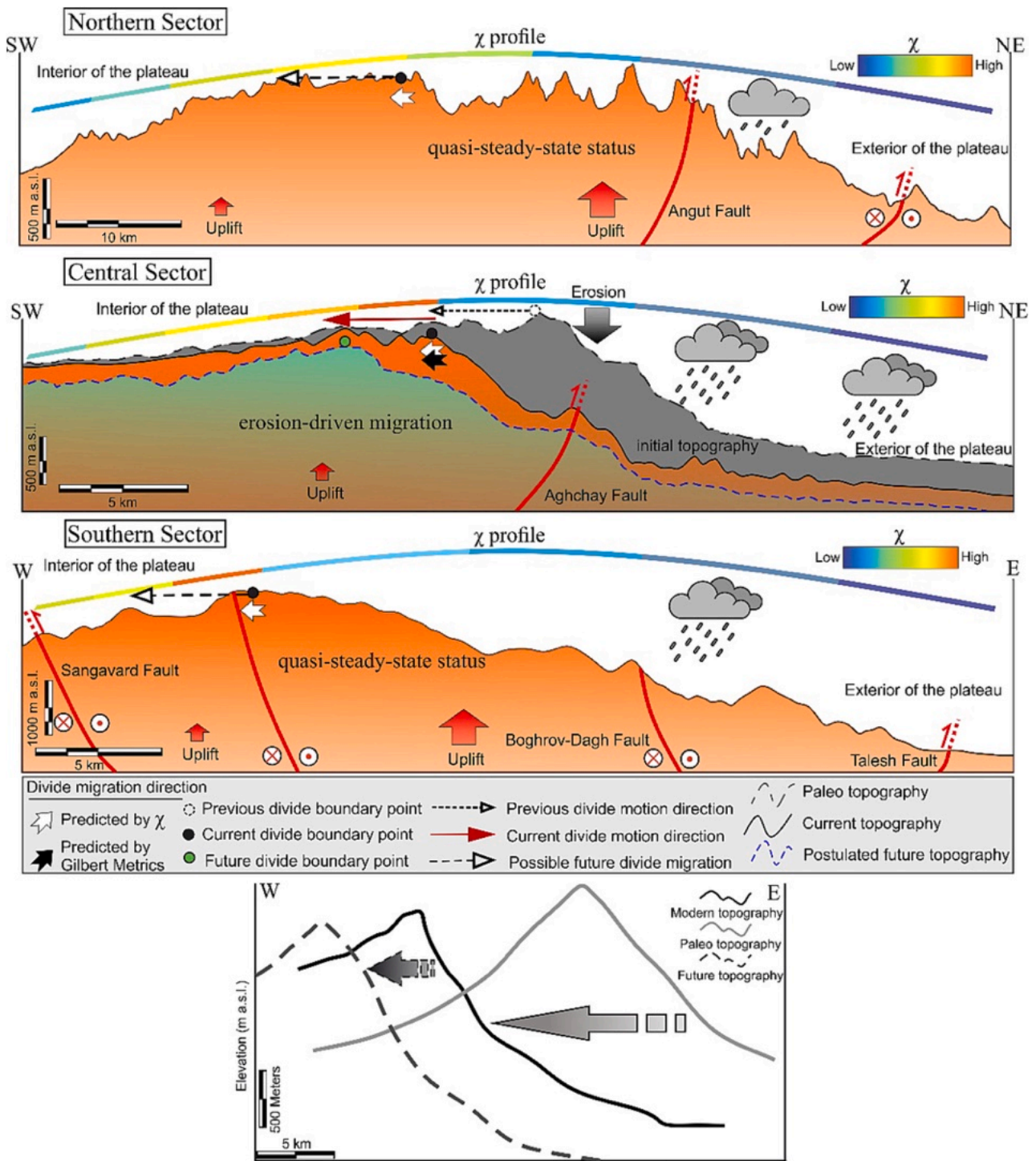
Fig. 17. The general topographic architecture of the Talesh Mts. in its north, central, and southern sectors. Postulated topography of the range, and a simple landscape evolution model of the study area. Green and grey-shaded areas represent the postulated future and paleo topography, respectively. In the northern sector, the rate of precipitation is lower than the central and southern sectors. In this sector due to higher uplift rate in Miocene and Pliocene respect to the central part, divide moved towards the high-uplift side and reached a quasi-steady state. In the central sector, the exposure of soft rock units along the divide, consequently greater contrasts in erodibility have driven faster drainage divide mobility rates. In this sector, a SW-dipping contact of pyroclastic and volcanic hard rocks (raised by rock uplift and shifted horizontally by topographic advection; Fig. 12d), alongside higher precipitation rate (Figs. 3b, and 15c) caused intensified drainage divide migration towards the interior of the plateau. Furthermore, the drainage divide in this sector was offset from the center of the range in the direction of advection towards southwest. The landscape in the southern sector developed in strong lithology (andesite) and seems to be in equilibrium suggested by Gilbert metrics. Similar to the northern sector, the rate of uplift and exhumation was higher in the south due to thrust and reverse faults, respect to the central sector. While the rate of precipitation, and χ contrast values is higher in the southern sector.

northern and southern parts. The χ metric is sensitive to this uplift rate gradient and representing the expected response of the divide when the uplift is evenly distributed. Furthermore, the Talesh Mts. which is undergoing active deformation indicates transient landscapes in the north and southern sectors which present an uplifted relict landscape, that has also represented in swath profiles, knickpoints with high elevation, and slope map. The divide in these sectors appears to be stable because the landscape across the divide is similar and has low topographic relief. On the other hand, the topography can also be significantly influenced by advection, which has caused the asymmetric topography of the central sector due to erosion of weaker lithology. Thus, contrasting exhumation of strong bedrock units in the northern and southern sectors, and weak bedrock units in the central sector have suppressed and intensified erosion, respectively, and this heterogeneous exhumation of rocks initiated topographic reconfiguration mostly in the central Talesh Mts. In addition to the mechanisms of the horizontal motion of rocks, the role of uplift of the mountains in middle Miocene, and Pliocene cannot be ruled out of mechanisms responsible for divide mobility.

CRediT authorship contribution statement

Mohammad Moumeni: Conceptualization, Data curation, Formal analysis, Investigation, Methodology, Project administration, Software, Visualization, Writing – original draft, Writing – review & editing. **Michele Delchiaro:** Conceptualization, Investigation, Methodology, Software, Writing – review & editing. **Marta Della Seta:** Conceptualization, Supervision, Writing – review & editing. **Reza Nozaem:** Writing – review & editing. **Paolo Ballato:** Conceptualization, Supervision, Writing – review & editing. **Joel S. Leonard:** Writing – review & editing. **Romano Clementucci:** Writing – review & editing. **Javad Rouhi:** Writing – review & editing.

Declaration of competing interest

The authors declare that they have no known competing financial interests or personal relationships that could have appeared to influence the work reported in this paper.

Data availability

Data will be made available on request through the corresponding author. The functions used in the analysis are available in *TopoToolbox*, *DivideTools*, and *TAK* (Topographic Analysis Kit). Details and general information on the rock samples used for UCS measurements are provided in the Supplementary materials.

Acknowledgments

Appendix A. Supplementary data

Supplementary data to this article can be found online at https://doi.org/10.1016/j.geomorph.2023.109029.

References

Adams, B.A., Whipple, K.X., Forte, A.M., Heimsath, A.M., Hodges, K.V., 2020. Climate controls on erosion in tectonically active landscapes. Sci. Adv. 6, eaaz3166 https://doi.org/10.1126/sciadv.aaz3166.

Agard, P., Omrani, J., Jolivet, L., Whitechurch, H., Vrielynck, B., Spakman, W., Wortel, R., 2011. Zagros orogeny: a subduction-dominated process. Geol. Mag. 148, 692–725.

Allen, M.B., Jones, S., Ismail-Zadeh, A., Simmons, M., Anderson, L., 2002. Onset of subduction as the cause of rapid Pliocene-Quaternary subsidence in the South Caspian basin. Geology 30 (9), 775–778.

Allen, M.B., Vincent, S.J., Alsop, G.I., Ismail-Zadeh, A., Flecker, R., 2003. Late Cenozoic deformation in the South Caspian region: effects of a rigid basement block within a collision zone. Tectonophysics 366, 223–239.

Allen, M., Jackson, J., Walker, R., 2004. Late Cenozoic re-organization of the Arabia-Eurasia collision and the comparison of short-term and long-term deformation rates. Tectonics 23, TC2008. https://doi.org/10.1029/2003TC001530.

Allen, G.H., Barnes, J.B., Pavelsky, T.M., Kirby, E., 2013. Lithologic and tectonic controls on bedrock channel form at the northwest Himalayan front. J. Geophys. Res. Earth 118 (3), 1806–1825. https://doi.org/10.1002/jgrf.20113.

ASTM, 2008. Standard Test Method for Determination of the Point Load Strength Index of Rock and Application to Rock Strength Classifications, 22. American Society for Testing and Materials Int, West Cochohocken, PA, pp. 51–60.

Axen, G.J., Lam, P.S., Grove, M., Stockli, D.F., Hassanzadeh, J., 2001. Exhumation of the west-central Alborz Mountains, Iran, Caspian subsidence, and collision-related tectonics. Geology 29 (6), 559–562.

Ballato, P., 2009. Tectonic and Climatic Forcing in Orogenic Processes: The Foreland Basin Point of View, Alborz Mountains, N Iran. Doctoral dissertation. Universität Potsdam.

Ballato, P., Strecker, M.R., 2014. Assessing tectonic and climatic causal mechanisms in foreland-basin stratal architecture: insights from the Alborz Mountains, northern Iran. Earth Surf. Process. Landf. 39 (1), 110–125.

Ballato, P., Nowaczyk, N.R., Landgraf, A., Strecker, M.R., Friedrich, A., Tabatabaei, S.H., 2008. Tectonic control on sedimentary facies pattern and sediment accumulation rates in the Miocene foreland basin of the southern Alborz mountains, northern Iran. Tectonics 27, TC6001. https://doi.org/10.1029/2008TC002278.

Ballato, P., Mulch, A., Landgraf, A., Strecker, M.R., Dalconi, M.C., Friedrich, A., Tabatabaei, S.H., 2010. Middle to late Miocene Middle Eastern climate from stable oxygen and carbon isotope data, southern Alborz mountains, N Iran. Earth Planet. Sci. Lett. 300 (1–2), 125–138.

Ballato, P., Uba, C.E., Landgraf, A., Strecker, M.R., Sudo, M., Stockli, D.F., Friedrich, A., Tabatabaei, S.H., 2011. Arabia-Eurasia continental collision: insights from late Tertiary foreland-basin evolution in the Alborz Mountains, northern Iran. Geol. Soc. Am. Bull. 123, 106–131.

Ballato, P., Stockli, D.F., Ghassemi, M.R., Landgraf, A., Strecker, M.R., Hassanzadeh, J., Friedrich, A., Tabatabaei, S.H., 2013. Accommodation of transpressional strain in the Arabia-Eurasia collision zone: new constraints from (U-Th)/He thermochronology in the Alborz mountains, N Iran. Tectonics 32, 1–18. https://doi.org/10.1029/2012TC003159.

Ballato, P., Landgraf, A., Schildgen, T.F., Stockli, D.F., Fox, M., Ghassemi, M.R., Kirby, E., Strecker, M.R., 2015. The growth of a mountain belt forced by base-level fall: tectonics and surface processes during the evolution of the Alborz Mountains, N Iran. Earth Planet. Sci. Lett. 425, 204–218. https://doi.org/10.1016/j.epsl.2015.05.051.

Ballato, P., Cifelli, F., Heidarzadeh, G., Ghassemi, M.R., Wickert, A.D., Hassanzadeh, J., Dupont-Nivet, G., Balling, P., Sudo, M., Zeilinger, G., Schmitt, A.K., 2017. Tectono-sedimentary evolution of the northern Iranian Plateau: insights from middle–late Miocene foreland-basin deposits. Basin Res. 29 (2), 417–446.

Berberian, M., 1983. The southern Caspian: a compressional depression floored by a trapped, modified oceanic crust. Can. J. Earth Sci. 20, 163–183.

Berberian, M., King, G.C.P., 1981. Towards a paleogeography and tectonic evolution of Iran. Can. J. Earth Sci. 5, 101–117.

Bookhagen, B., Strecker, M.R., 2012. Spatiotemporal trends in erosion rates across a pronounced rainfall gradient: examples from the southern Central Andes. Earth Planet. Sci. Lett. 327, 97–110.

Broch, E., Franklin, J.A., 1972. The point-load strength test. In: International Journal of Rock Mechanics and Mining Sciences & Geomechanics Abstracts, Vol. 9, No. 6. Pergamon, pp. 669–676.

Burbank, D.W., Blythe, A.E., Putkonen, J., Pratt-Sitaula, B.G.A.B.E.T., Gabet, E., Oskin, M., Barros, A., Ojha, T.P., 2003. Decoupling of erosion and precipitation in the Himalayas. Nature 426 (6967), 652–655.

Bursztyn, N., Pederson, J.L., Tressler, C., Mackley, R.D., Mitchell, K.J., 2015. Rock strength along a fluvial transect of the Colorado Plateau – quantifying a fundamental control on geomorphology. Earth Planet. Sci. Lett. 429, 90–100. https://doi.org/10.1016/j.epsl.2015.07.042.

Buscher, J.T., Ascione, A., Valente, E., 2017. Decoding the role of tectonics, incision and lithology on drainage divide migration in the Mt. Alpi region, southern Apennines, Italy. Geomorphology 276, 37–50.

Calvet, M., Gunnell, Y., Farines, B., 2015. Flat-topped mountain ranges: their global distribution and value for understanding the evolution of mountain topography. Geomorphology 241, 255–291. https://doi.org/10.1016/j.geomorph.2015.04.015.

Campforts, B., Vanacker, V., Herman, F., Vanmaercke, M., Schwanghart, W., Tenorio, G.E., 2020. Parameterization of river incision models requires accounting for environmental heterogeneity: insights from the tropical Andes. Earth Surf. Dyn. 8 (2), 447–470. https://doi.org/10.5194/esurf-8-447-2020.

Chilton, K.D., 2021. Point load testing to more effectively measure bedrock strength. Nat. Rev. Earth Environ. 0123456789 (7), 43017 https://doi.org/10.1038/s43017-021-00180-w.

Chilton, K.D., Spotila, J.A., 2022. Uncovering the controls on fluvial bedrock erodibility and knickpoint expression: a high-resolution comparison of bedrock properties between knickpoints and non-knickpoint reaches. J. Geophys. Res. Earth 127 (3), e2021JF006511.

Clark, M.K., Royden, L.H., Whipple, K.X., Burchfiel, B.C., Zhang, X., Tang, W., 2006. Use of a regional, relict landscape to measure vertical deformation of the eastern Tibetan Plateau. J. Geophys. Res. 111, F03002 https://doi.org/10.1029/2005JF000294.

Clementucci, R., Ballato, P., Siame, L.L., Faccenna, C., Yaaqoub, A., Essaifi, A., Leanni, L., Guillou, V., 2022. Lithological control on topographic relief evolution in a slow tectonic setting (Anti-Atlas, Morocco). Earth Planet. Sci. Lett. 596, 117788.

Clementucci, R., Ballato, P., Siame, L.L., Faccenna, C., Racano, S., Torreti, G., Lanari, R., Leanni, L., Guillou, V., 2023. Transient response to changes in uplift rates in the northern Atlas-Meseta system (Morocco). Geomorphology 436, 108765.

Davoudzadeh, M., Lammerer, B., Weber-Diefenbach, K., 1997. Paleogeography, stratigraphy, and tectonics of the tertiary of Iran. N. Jb. Geol. Palaont. Abh. 205, 33–67.

Delchiaro, M., Iacobucci, G., Troiani, F., Della Seta, M., Ballato, P., Aldega, L., 2022. Morphoevolution of the Seymareh landslide-dam lake system (Zagros Mountains, Iran): implications for Holocene climate and environmental changes. Geomorphology 413, 108367.

Delchiaro, M., Della Seta, M., Martino, S., Nozaem, R., Moumeni, M., 2023. Tectonic deformation and landscape evolution inducing mass rock creep driven landslides: the Loumar case-study (Zagros Fold and Thrust Belt, Iran). Tectonophysics 846, 229655.

DiBiase, R.A., Denn, A.R., Bierman, P.R., Kirby, E., West, N., Hidy, A.J., 2018. Stratigraphic control of landscape response to base-level fall, YoungWomans Creek, Pennsylvania, USA. Earth Planet. Sci. Lett. 504, 163–173. https://doi.org/10.1016/j.epsl.2018.10.005.

Djamour, Y., Vernant, P., Bayer, R., Nankali, H.R., Ritz, J.F., Hinderer, J., Hatam, Y., Luck, B., Le Moigne, N., Sedighi, M., Khorrami, F., 2010. GPS and gravity constraints on continental deformation in the Alborz mountain range, Iran. Geophys. J. Int. 183 (3), 1287–1301.

Djamour, Y., Vernant, P., Nankali, H.R., Tavakoli, F., 2011. NW Iran-eastern Turkey present-day kinematics: results from the Iranian permanent GPS network. Earth Planet. Sci. Lett. 307, 27–34.

Duvall, A., Kirby, E., Burbank, D., 2004. Tectonic and lithologic controls on bedrock channel profiles and processes in coastal California. J. Geophys. Res. Earth 109 (F3). https://doi.org/10.1029/2003JF000086.

Expósito, I., Jiménez-Bonilla, A., Delchiaro, M., Yanes, J.L., Balanyá, J.C., Moral-Martos, F. Della, Seta, M., 2022. Geomorphic signature of segmented relief rejuvenation in the Sierra Morena, Betic forebulge, Spain. Earth Surf. Dyn. 10 (5), 1017–1039.

Farr, T.G., Rosen, P.A., Caro, E., Crippen, R., Duren, R., Hensley, S., Kobrick, M., Paller, M., Rodriguez, E., Roth, L., Seal, D., 2007. The shuttle radar topography mission. Rev. Geophys. 45 (2).

Ferrier, K.L., Huppert, K.L., Perron, J.T., 2013. Climatic control of bedrock river incision. Nature 496, 206–209. https://doi.org/10.1038/nature11982.

Fick, S.E., Hijmans, R.J., 2017. WorldClim 2: new 1-km spatial resolution climate surfaces for global land areas. Int. J. Climatol. 37 (12), 4302–4315.

Finlayson, D.P., Montgomery, D.R., Hallet, B., 2002. Spatial coincidence of rapid inferred erosion with young metamorphic massifs in the Himalayas. Geology 30 (3), 219–222.

Flint, J.J., 1974. Stream gradient as a function of order, magnitude, and discharge. Water Resour. Res. 10, 969–973.

Forte, A.M., Cowgill, E., 2013. Late Cenozoic base-level variations of the Caspian Sea: a review of its history and proposed driving mechanisms. Palaeogeogr. Palaeoclimatol. Palaeoecol. 386, 392–407.

Forte, A.M., Whipple, K.X., 2018. Criteria and tools for determining drainage divide stability. Earth Planet. Sci. Lett. 493, 102–117. https://doi.org/10.1016/j.epsl.2018.04.026.

Forte, A.M., Whipple, K.X., 2019. The topographic analysis kit (TAK) for TopoToolbox. Earth Surf. Dyn. 7 (1), 87–95.

Forte, A.M., Yanites, B.J., Whipple, K.X., 2016. Complexities of landscape evolution during incision through layered stratigraphy with contrasts in rock strength. Earth Surf. Process. Landf. 41 (12), 1736–1757. https://doi.org/10.1002/esp.3947.

Fox, M., 2019. A linear inverse method to reconstruct paleo-topography. Geomorphology 337, 151–164. https://doi.org/10.1016/j.geomorph.2019.03.034.

Franklin, J.A., 1985. Suggested method for determining point load strength. Int. J. Rock Mech. Min. Sci. 22 (2), 51–60. https://doi.org/10.1016/0148-9062(85)92327-7.

Gallen, S.F., 2018. Lithologic controls on landscape dynamics and aquatic species evolution in post-orogenic mountains. Earth Planet. Sci. Lett. 493, 150–160. https://doi.org/10.1016/j.epsl.2018.04.029.

Gallen, S.F., Wegmann, K.W., 2017. River profile response to normal fault growth and linkage: an example from the Hellenic forearc of south-central Crete, Greece. Earth Surf. Dyn. 5 (1), 161–186. https://doi.org/10.5194/esurf-5-161-2017.

Geological Survey of Iran, 1975. Geological Quadrangle Map of Iran, Masuleh Sheet, Scale 1:100,000, edited by R. G. Davis et al, Geological Survey of Iran, Tehran.

Geological Survey of Iran, 1999. Geological Quadrangle Map of Iran, Kivi Sheet, Scale 1:100,000. In: Hajialilo, B. (Ed.), and H. Rezaei, Geological Survey of Iran, Tehran.

Ghorbani, M., 2013. A summary of geology of Iran. In: The Economic Geology of Iran. Springer, Dordrecht, pp. 45–64.

Giachetta, E., Refice, A., Capolongo, D., Gasparini, N.M., Pazzaglia, F.J., 2014. Orogen-scale drainage network evolution and response to erodibility changes: insights from numerical experiments. Earth Surf. Process. Landf. 39, 1259–1268. https://doi.org/10.1002/esp.3579.

Gilbert, G.K., 1877. Geology of the Henry Mountains. Government Printing Office, pp. i–160.

Goudie, A.S., 2006. The Schmidt Hammer in geomorphological research. Prog. Phys. Geogr. 30 (6), 703–718. https://doi.org/10.1177/0309133306071954.

Guest, B., Axen, G.J., Lam, P.S., Hassanzadeh, J., 2006. Late Cenozoic shortening in the west-central Alborz Mountains, northern Iran, by combined conjugate strike-slip and thin-skinned deformation. Geosphere 2 (1), 35–52.

Hack, J.T., 1957. Studies of Longitudinal Stream Profiles in Virginia and Maryland, vol. 294. US Government Printing Office.

Hancock, G., Kirwan, M., 2007. Summit erosion rates deduced from 10Be: Implications for relief production in the central Appalachians. Geology 35 (1), 89–92. https://doi.org/10.1130/G23147A.1.

He, C., Yang, C.-J., Turowski, J.M., Rao, G., Roda-Boluda, D.C., Yuan, X.-P., 2021. Constraining tectonic uplift and advection fromthe main drainage divide of a mountain belt. Nat. Commun. 12 (1), 544. Available from: https://doi.org/10.1038/s41467-020-20748-2.

Hoek, E., Brown, E.T., 1997. Practical estimates of rock mass strength. Int. J. Rock Mech. Min. Sci. 34 (8), 1165–1186.

Hoek, E., Carter, T.G., Diederichs, M.S., 2013. Quantification of the geological strength index chart. In: ARMA US Rock Mechanics/Geomechanics Symposium (pp. ARMA-2013). ARMA.

Jackson, M.P.A., Cornelius, R.R., Craig, C.H., Gansser, A., Stöcklin, J., Talbot, C.J., 1990. Salt diapirs of the Great Kavir, Central Iran. In: Boulder, Geological Society of America Memoir, v. 177. Geological Society of America, 139 p.

Jackson, J., Priestley, K., Allen, M., Berberian, M., 2002. Active tectonics of the South Caspian Basin. Geophys. J. Int. 148, 214–245.

Keller, E.A., Pinter, N., 2002. Active Tectonics: Earthquakes, Uplift, and Landscape (No Title).

Kirby, E., Whipple, K., 2001. Quantifying differential rock-uplift rates via stream profile analysis. Geology 29 (5), 415–418. https://doi.org/10.1130/0091-7613(2001)029<0415:QDRURV>2.0.CO;2.

Kirby, E., Whipple, K.X., 2012. Expression of active tectonics in erosional landscapes. J. Struct. Geol. 44, 54–75. https://doi.org/10.1016/j.jsg.2012.07.009.

Kirby, E., Whipple, K.X., Tang, W., Chen, Z., 2003. Distribution of active rock uplift along the eastern margin of the Tibetan Plateau: inferences from bedrock channel longitudinal profiles. J. Geophys. Res. Solid Earth 108 (B4). https://doi.org/10.1029/2001JB000861.

Lague, D., 2014. The stream power river incision model: evidence, theory and beyond. Earth Surf. Process. Landf. 39 (1), 38–61.

Leonard, J.S., Whipple, K.X., 2021. Influence of spatial rainfall gradients on river longitudinal profiles and the topographic expression of spatially and temporally variable climates in mountain landscapes. J. Geophys. Res. Earth 126 (12), e2021JF006183.

Leonard, J.S., Whipple, K.X., Heimsath, A.M., 2023. Isolating climatic, tectonic, and lithologic controls on mountain landscape evolution. Sci. Adv. 9 (3), eadd8915.

Madanipour, S., 2023. Late Miocene–early Pliocene transition to erosional exhumation in the northwest of the Arabia–Eurasia collision zone. Earth Surf. Process. Landf. 48, 1724–1741. https://doi.org/10.1002/esp.5583.

Madanipour, S., Ehlers, T.A., Yassaghi, A., Rezaeian, M., Enkelmann, E., Bahroudi, A., 2013. Synchronous deformation on orogenic plateau margins: Insights from the Arabia–Eurasia collision. Tectonophysics 608, 440–451.

Madanipour, S., Ehlers, T.A., Yassaghi, A., Enkelmann, E., 2017. Accelerated middle Miocene exhumation of the Talesh Mountains constrained by U-Th/He thermochronometry: evidence for the Arabia-Eurasia collision in the NW Iranian Plateau. Tectonics 36 (8), 1538–1561.

Madanipour, S., Yassaghi, A., Ehlers, T.A., Enkelmann, E., 2018. Tectonostratigraphy, structural geometry and kinematics of the NW Iranian Plateau margin: insights from the Talesh Mountains, Iran. Am. J. Sci. 318 (2), 208–245.

Maneerat, P., Bürgmann, R., 2022. Geomorphic expressions of active tectonics across the Indo-Burma Range. J. Asian Earth Sci. 223, 105008.

McQuarrie, N., van Hinsbergen, D.J., 2013. Retrodeforming the Arabia-Eurasia collision zone: age of collision versus magnitude of continental subduction. Geology 41 (3), 315–318.

Miller, S.R., Sak, P.B., Kirby, E., Bierman, P.R., 2013. Neogene rejuvenation of central Appalachian topography: evidence for differential rock uplift from stream profiles and erosion rates. Earth Planet. Sci. Lett. 369, 1–12.

Mills, H.H., 2003. Inferring erosional resistance of bedrock units in the east Tennessee mountains from digital elevation data. Geomorphology 55, 263–281.

Mitchell, N., Forte, A.M., 2023. Tectonic advection of contacts enhances landscape transience. Earth Surf. Process. Landf. https://doi.org/10.1002/esp.5559.

Molnar, P., Anderson, R.S., Anderson, S.P., 2007. Tectonics, fracturing of rock, and erosion. J. Geophys. Res. Earth 112 (F3).

Montgomery, D.R., Balco, G., Willett, S.D., 2001. Climate, tectonics, and the morphology of the Andes. Geology 29 (7), 579–582.

Moumeni, M., Delchiaro, M., Della Seta, M., Nozaem, R., 2022. Asymmetric Uplift in the NW Iranian Plateau: An Insight from the Dynamic Divide Migration of Ardebil Basin, No. ICG2022-120. Copernicus Meetings.

Mouthereau, F., Lacombe, O., Vergés, J., 2012. Building the Zagros collisional orogen: timing, strain distribution and the dynamics of Arabia/Eurasia plate convergence. Tectonophysics 532–535, 27–60. https://doi.org/10.1016/j.tecto.2012.01.022.

Murphy, B.P., Johnson, J.P.L., Gasparini, N.M., Hancock, G.S., Small, E.E., 2018. Weathering and abrasion of bedrock streambed topography. Geology 46 (5), 459–462. https://doi.org/10.1130/G40186.1.

Olivetti, V., Godard, V., Bellier, O., ASTER team, 2016. Cenozoic rejuvenation events of Massif Central topography (France): Insights from cosmogenic denudation rates and river profiles. Earth Planet. Sci. Lett. 444, 179–191. https://doi.org/10.1016/j.epsl.2016.03.049.

Pérez-Peña, J.V., Al-Awabdeh, M.O.H.A.M.M.A.D., Azañón, J.M., Galve, J.P., Booth-Rea, G., Notti, D., 2017. SwathProfiler and NProfiler: two new ArcGIS Add-ins for the automatic extraction of swath and normalized river profiles. Comput. Geosci. 104, 135–150.

Perron, J.T., Royden, L., 2013. An integral approach to bedrock river profile analysis. Earth Surf. Process. Landf. 38 (6), 570–576. https://doi.org/10.1002/esp.3302.

Pike, R.J., Wilson, S.E., 1971. Elevation-relief ratio, hypsometric integral, and geomorphic area-altitude analysis. Geol. Soc. Am. Bull. 82 (4), 1079–1084.

Racano, S., Schildgen, T.F., Cosentino, D., Miller, S.R., 2021. Temporal and spatial variations in rock uplift from river-profile inversions at the Central Anatolian Plateau southern margin. J. Geophys. Res. Earth 126 (8), e2020JF006027. https://doi.org/10.1029/2020JF006027.

Racano, S., Schildgen, T., Ballato, P., Yıldırım, C., Wittmann, H., 2023. Rock-uplift history of the Central Pontides from river-profile inversions and implications for development of the North Anatolian Fault. Earth Planet. Sci. Lett. 616, 118231.

Reilinger, R., McClusky, S., Vernant, P., Lawrence, S., Ergintav, S., Cakmak, R., Ozener, H., Kadirov, F., Guliev, I., Stepanyan, R., Nadariya, M., 2006. GPS constraints on continental deformation in the Africa-Arabia-Eurasia continental collision zone and implications for the dynamics of plate interactions. J. Geophys. Res. Solid Earth 111 (B5).

Roe, G.H., 2005. Orographic precipitation. Annu. Rev. Earth Planet. Sci. 33 (1), 645–671. https://doi.org/10.1146/annurev. earth.33.092203.122541.

Scherler, D., Schwanghart, W., 2020. Drainage divide networks–part 1: identification and ordering in digital elevation models. Earth Surf. Dyn. 8 (2), 245–259.

Schildgen, T.F., Cosentino, D., Bookhagen, B., Niedermann, S., Yıldırım, C., Echtler, H., Wittmann, H., Strecker, M.R., 2012. Multi-phased uplift of the southern margin of the Central Anatolian plateau, Turkey: a record of tectonic and upper mantle processes. Earth Planet. Sci. Lett. 317, 85–95. https://doi.org/10.1016/j.epsl.2011.12.003.

Schmidt, K.M., Montgomery, D.R., 1995. Limits to relief. Science 270 (5236), 617–620.

Schwanghart, W., Scherler, D., 2014. TopoToolbox 2–MATLAB-based software for topographic analysis and modeling in Earth surface sciences. Earth Surf. Dyn. 2 (1), 1–7. https://doi.org/10.5194/esurf-2-1-2014.

Schwanghart, W., Scherler, D., 2017. Bumps in river profiles: uncertainty assessment and smoothing using quantile regression techniques. Earth Surf. Dyn. 5, 821–839. https://doi.org/10.5194/esurf-5-821-2017.

Shobe, C.M., Hancock, G.S., Eppes, M.C., Small, E.E., 2017. Field evidence for the influence of weathering on rock erodibility and channel form in bedrock rivers. Earth Surf. Process. Landf. 42 (13), 1997–2012. https://doi.org/10.1002/esp.4163.

Sinclair, H.D., Mudd, S.M., Dingle, E., Hobley, D.E.J., Robinson, R., Walcott, R., 2017. Squeezing river catchments through tectonics: shortening and erosion across the Indus Valley, NW Himalaya. Geol. Soc. Am. Bull. 129 (1–2), 203–217. Available from: https://doi.org/10.1130/B31435.1.

Snyder, N.P., Whipple, K.X., Tucker, G.E., Merritts, D.J., 2000. Landscape response to tectonic forcing: digital elevation model analysis of stream profiles in the Mendocino triple junction region, northern California. Geol. Soc. Am. Bull. 112 (8), 1250–1263. https://doi.org/10.1130/0016-7606(2000)112<1250:LRTTFD>2.0.CO;2.

Stocklin, J., 1968. Structural history and tectonics of Iran: a review. Am. Assoc. Pet. Geol. Bull. 52, 1229–1258.

Su, Q., Wang, X., Lu, H., Xie, H., 2020. Dynamic divide migration as a response to asymmetric uplift: an example from the Zhongtiao Shan, North China. Remote Sens. 12 (24), 4188.

Townsend, M., 2022. Linking surface deformation to thermal and mechanical magma chamber processes. Earth Planet. Sci. Lett. 577, 117272.

Vernant, P., Nilforoushan, F., Hatzfeld, D., Abbassi, M.R., Vigny, C., Masson, F., Nankali, H., Martinod, J., Ashtiani, A., Bayer, R., Tavakoli, F., 2004. Present-day crustal deformation and plate kinematics in the Middle East constrained by GPS measurements in Iran and northern Oman. Geophys. J. Int. 157 (1), 381–398.

Vincent, S.J., Allen, M.B., Ismail-Zadeh, A.D., Flecker, R., Foland, K.A., Simmons, M.D., 2005. Insights from the Talysh of Azerbaijan into the Paleogene evolution of the South Caspian region. Geol. Soc. Am. Bull. 117 (11–12), 1513–1533.

Walpersdorf, A., Manighetti, I., Mousavi, Z., Tavakoli, F., Vergnolle, M., Jadidi, A., Hatzfeld, D., Aghamohammadi, A., Bigot, A., Djamour, Y., Nankali, H., 2014. Present-day kinematics and fault slip rates in eastern Iran, derived from 11 years of GPS data. J. Geophys. Res. Solid Earth 119 (2), 1359–1383.

Whipple, K.X., 2004. Bedrock rivers and the geomorphology of active orogens. Annu. Rev. Earth Planet. Sci. 32, 151–185. https://doi.org/10.1146/annurev. earth.32.101802.120356.

Whipple, K.X., 2009. The influence of climate on the tectonic evolution of mountain belts. Nat. Geosci. 2 (2), 97–104.

Whipple, K.X., Tucker, G.E., 1999. Dynamics of the stream-power river incision model: implications for height limits of mountain ranges, landscape response timescales, and research needs. J. Geophys. Res. Solid Earth 104 (B8), 17661–17674. https://doi.org/10.1029/1999JB900120.

Whipple, K.X., DiBiase, R.A., Crosby, B.T., 2013. Bedrock rivers. In: Treatise on Geomorphology, vol. 9, pp. 550–573.

Whipple, K.X., DiBiase, R.A., Ouimet, W.B., Forte, A.M., 2017. Preservation or piracy: diagnosing low-relief, high-elevation surface formation mechanisms. Geology 45 (1), 91–94. https://doi.org/10.1130/G38490.1.

Whipple, K.X., DiBiase, R.A., Crosby, B., Johnson, J.P., 2022. Bedrock rivers. In: Treatise on Geomorphology. Elsevier, pp. 865–903.

Willett, S.D., 1999. Orogeny and orography: the effects of erosion on the structure of mountain belts. J. Geophys. Res. Solid Earth 104 (B12), 28957–28981.

Willett, S.D., Slingerland, R., Hovius, N., 2001. Uplift, shortening, and steady state topography in active mountain belts. Am. J. Sci. 301 (4–5), 455–485. Available from: https://doi.org/10.2475/ajs.301.4-5.455.

Willett, S.D., McCoy, S.W., Perron, J.T., Goren, L., Chen, C.Y., 2014. Dynamic reorganization of river basins. Science 343 (6175). https://doi.org/10.1126/science.1248765.

Winterberg, S., Willett, S.D., 2019. Greater Alpine river network evolution, interpretations based on novel drainage analysis. Swiss J. Geosci. 112, 3–22.

Wobus, C., Whipple, K.X., Kirby, E., Snyder, N., Johnson, J., Spyropolou, K., Crosby, B., Sheehan, D., 2006. Tectonics from topography: procedures, promise, and pitfalls. Geol. Soc. Am. Spec. Pap. 398, 55. https://doi.org/10.1130/2006.2398(04).

Wobus, C.W., Whipple, K.X., Hodges, K.V., 2006b. Neotectonics of the central Nepalese Himalaya: constraints from geomorphology, detrital 40Ar/39Ar thermochronology, and thermal modeling. Tectonics 25 (4).

Yang, R., Willett, S.D., Goren, L., 2015. In situ low-relief landscape formation as a result of river network disruption. Nature 520 (7548), 526–529.

Yassaghi, A., Madanipour, S., 2008. Influence of a transverse basement fault on along-strike variations in the geometry of an inverted normal fault: case study of the Mosha Fault, Central Alborz Range, Iran. J. Struct. Geol. 30 (12), 1507–1519.

Ye, Y., Tan, X., Zhou, C., 2022. Initial topography matters in drainage divide migration analysis: insights from numerical simulations and natural examples. Geomorphology 409, 108266.

Zaitchik, B.F., Evans, J.P., Smith, R.B., 2007. Regional impact of an elevated heat source: the Zagros Plateau of Iran. J. Clim. 20 (16), 4133–4146.

Zondervan, J.R., Whittaker, A.C., Bell, R.E., Watkins, S.E., Brooke, S.A.S., Hann, M.G., 2020a. New constraints on bedrock erodibility and landscape response times upstream of an active fault. Geomorphology 351, 106937. https://doi.org/10.1016/j.geomorph.2019.106937.

Zondervan, J.R., Stokes, M., Boulton, S.J., Telfer, M.W., Mather, A.E., 2020b. Rock strength and structural controls on fluvial erodibility: implications for drainage divide mobility in a collisional mountain belt. Earth Planet. Sci. Lett. 538, 116221 https://doi.org/10.1016/j.epsl.2020.116221.